



# Radiative forcing of anthropogenic aerosols on cirrus clouds using a hybrid ice nucleation scheme

Jialei Zhu<sup>1,2</sup> and Joyce E. Penner<sup>2</sup>

<sup>1</sup>Institute of Surface-Earth System Science, School of Earth System Science, Tianjin University, Tianjin 300072, China

<sup>2</sup>Department of Climate and Space Sciences and Engineering, University of Michigan, Ann Arbor, Michigan 48109, USA

**Correspondence:** Jialei Zhu (zhujialei@tju.edu.cn)

Received: 14 November 2019 – Discussion started: 3 January 2020

Revised: 16 May 2020 – Accepted: 26 May 2020 – Published: 3 July 2020

**Abstract.** Anthropogenic aerosols impact cirrus clouds through ice nucleation, thereby changing the Earth's radiation budget. However, the magnitude and sign of anthropogenic forcing in cirrus clouds is still very uncertain depending on the treatments for ice-nucleating particles (INPs), the treatments for haze particle freezing, and the ice nucleation scheme. In this study, a new ice nucleation scheme (hereafter the HYBRID scheme) is developed to combine the best features of two previous ice nucleation schemes, so that global models are able to calculate the ice number concentration in both updrafts and downdrafts associated with gravity waves, and it has a robust sensitivity to the change of aerosol number. The scheme is applied in a box model, and the ice number concentrations ( $9.52 \pm 2.08 \text{ L}^{-1}$ ) are somewhat overestimated but are in reasonable agreement with those from an adiabatic parcel model ( $9.40 \pm 2.31 \text{ L}^{-1}$ ). Then, the forcing and cloud changes associated with changes in aircraft soot, sulfur emission, and all anthropogenic emissions between the preindustrial (PI) period and the present day (PD) are examined using the CESM/IMPACT global model with the HYBRID scheme. Aircraft soot emissions decrease the global average ice number concentration ( $N_i$ ) by  $-1.0 \pm 2.4 \times 10^7 \text{ m}^{-2}$  ( $-1\%$ ) (over the entire column) due to the inhibition of homogeneous nucleation and lead to a radiative forcing of  $-0.14 \pm 0.07 \text{ W m}^{-2}$ , while the increase in sulfur emissions increases the global average  $N_i$  by  $7.3 \pm 2.9 \times 10^7 \text{ m}^{-2}$  ( $5\%$ ) due to the increase in homogeneous nucleation and leads to a radiative forcing of  $-0.02 \pm 0.06 \text{ W m}^{-2}$ . The possible effects of aerosol and cloud feedbacks to the meteorological state in remote regions partly contribute to reduce the forcing and the change in  $N_i$  due to anthropogenic emissions. The radiative forcing due

to all increased anthropogenic emissions from PI to PD is estimated to be  $-0.20 \pm 0.05 \text{ W m}^{-2}$ . If newly formed secondary organic aerosols (SOAs) act as INPs and inhibit homogeneous nucleation, the  $N_i$  formed from heterogeneous nucleation is increased. As a result, the inclusion of INPs from SOA increases the change in  $N_i$  to  $12.0 \pm 2.3 \times 10^7 \text{ m}^{-2}$  ( $9\%$ ) and increases (makes less negative) the anthropogenic forcing on cirrus clouds to  $-0.04 \pm 0.08 \text{ W m}^{-2}$  from PI to PD.

## 1 Introduction

Atmospheric aerosol loading has increased significantly since the preindustrial (PI) period, mainly due to anthropogenic emissions associated with the burning of fossil fuels and biomass. Most studies to date have focused on how the increase in anthropogenic aerosols impacts climate via warm clouds, thereby exerting a net cooling effect (Wang and Penner, 2009; Zhu et al., 2019; Gordon et al., 2016; IPCC, 2013). Compared to warm clouds, there has been much less attention paid to anthropogenic forcing as a result of changes to cirrus clouds, which is one of the least understood processes in the climate system (Fan et al., 2016). Cirrus clouds cover about 30% of the Earth's area (Wang et al., 1996) and play an important role in the Earth's radiation budget and also influence global precipitation and the hydrologic cycle (Waliser et al., 2009; Hong et al., 2016; Matus and L'Ecuyer 2017). Ice particles in cirrus clouds are nucleated on aerosol particles, so that changes to the aerosol composition and loading may alter cirrus clouds by altering cloud microphysics, resulting in a cirrus cloud radiative forcing.

There are major uncertainties in calculating the radiative forcing of cirrus clouds using global climate models, in terms of both its magnitude (since PI) and its sign (Storelvmo, 2017). The ice particles in the cirrus clouds can form either by homogeneous freezing of solution droplets (or haze particles) (Koop et al., 2000) or by heterogeneous nucleation of ice-nucleating particles (INPs; Cantrell and Heymsfield, 2005). Supercooled aqueous solutions such as sulfate haze particles can form ice through homogeneous nucleation when the relative humidity with respect to ice ( $RH_i$ ) is high (of the order of 150 %), which may be the dominant mechanism for the ice formation in cirrus clouds (Hendricks et al., 2011; Kuebbeler et al., 2014; Penner et al., 2018). However, heterogeneous ice nucleation of INPs formed from dust, soot, and other insoluble aerosols requires much lower  $RH_i$ , so that heterogeneous nucleation is able to occur in advance of homogeneous nucleation in a rising air parcel (Hoose and Möhler, 2012). As a result, heterogeneous and homogeneous ice formation compete for the available water vapor. Heterogeneous nucleation can lead to a significant reduction of the number of ice particles that form compared to homogeneous freezing because the number of INPs is much smaller than the number of haze particles. However, if additional INPs are added to a region where heterogeneous nucleation already dominates, an increase in ice crystal number is expected. Therefore, the radiative effect of aerosols on cirrus clouds could differ in both magnitude and sign depending on the competition between these two ice nucleation processes. Ice nucleation by INPs vs. haze freezing is determined by both the number of homogeneous and heterogeneous ice-nucleating particles and the updraft velocity or cooling rate.

Despite the relatively low level of understanding of ice nucleation, a few physically based parameterizations that treat the competition between homogeneous and heterogeneous nucleation have been developed in order to study the effect of ice nucleation in global climate models (Liu and Penner, 2005; Kärcher et al., 2006; Barahona and Nenes, 2008). The Liu and Penner (2005) parameterization (hereafter LP) is derived from fitting the simulation results of an adiabatically rising cloud parcel (Liu and Penner, 2005). The LP parameterization is only able to treat cases for which the updraft velocity is positive, so the evaporation of drops during downdrafts is neglected. The parameterization developed by Barahona and Nenes (2008) (hereafter BN) is derived from an analytical solution of the cloud parcel equations (Barahona and Nenes, 2008). The LP and BN parameterizations always show a similar trend when there is an increase in either the haze aerosol number concentrations or INPs (Shi and Liu, 2018), and they result in very similar ice number concentrations when the water vapor accommodation coefficient is set to 0.1 (Zhou et al., 2016). The Kärcher et al. (2006) parameterization (hereafter KL) explicitly calculates the evolution of ice supersaturation in a rising cloud parcel when different aerosol types freeze (Kärcher et al., 2006). The KL parameterization was used in previous studies on the effect of

aerosol particles on cirrus clouds because it includes an explicit representation of the relevant physics (Penner et al., 2009, 2018), and Penner et al. (2018) added the capability to represent evaporation of water in downdrafts. However, in the KL parameterization, aerosol particles in different size bins will freeze chronologically from the largest size bin until the rate at which  $RH_i$  decreases by water vapor deposition equals the rate at which  $RH_i$  increases as a result of temperature decreases. Under this assumption, competition among different aerosol size bins for water deposition is not allowed. As a result, the homogeneous freezing of some particles in small size bins is underestimated in the KL parameterization (Liu and Shi, 2018). The KL parameterization results in a smaller sensitivity to increases in sulfate aerosol number than the LP and BN parameterizations except at very low sulfate number concentrations, while the three parameterizations have similar sensitivity to the number concentration of INPs (Shi and Liu, 2018).

Global numerical simulation experiments of aerosol effects on cirrus cloud formation have been carried out in a limited number of studies with different ice nucleation parameterizations and updraft treatments. Penner et al. (2009) used the KL and LP parameterizations to estimate the radiative forcing of aerosols on cirrus clouds using an offline ice nucleation and radiative transfer model. They found a negligible forcing from sulfate but a significant cooling (ranging from  $-0.38$  to  $-0.56 \text{ W m}^{-2}$ ) from surface-based and aircraft emissions of soot with the assumption that 100 % of soot particles are efficient INPs (Penner et al., 2009). As a result, the radiative forcing of all anthropogenic aerosols was estimated to be  $-0.53$  to  $-0.67 \text{ W m}^{-2}$  using the LP and KL parameterizations. However, observations later indicated that only 0.01 % to 0.1 % of the less-hygroscopic soot from fossil fuels and biomass fires acts as good INPs at supersaturations near 140 %  $RH_i$  and low temperatures (Koehler et al., 2009; Pratt et al., 2011; Prenni et al., 2012). Gettelman et al. (2012) used the LP and BN parameterizations and calculated that the radiative forcing associated with aerosol effects on cirrus clouds is  $0.27 \pm 0.10 \text{ W m}^{-2}$  (the uncertainty is the standard deviation of the interannual variations hereafter) as a consequence of increasing anthropogenic sulfur emissions (with no effect from soot) (Gettelman et al., 2012).

In addition to assumptions of the extent to which soot might act as an INP, a second source of uncertainty in the calculation of aerosol forcing in cirrus clouds is the treatment of the sub-grid-scale updraft velocity used in the nucleation scheme (Zhou et al., 2016). Penner et al. (2009) used a normal probability distribution with a standard deviation of  $0.33 \text{ m s}^{-1}$  (Penner et al., 2009) while Wang and Penner (2010) used a single updraft velocity based on the standard deviation of mesoscale temperature fluctuations associated with gravity waves (Wang and Penner, 2010). Other models chose a sub-grid-scale updraft velocity associated with the predicted turbulent kinetic energy (Liu et al., 2012; Kärcher and Lohmann, 2002; Lohmann, 2002; Lohmann et

al., 1999). Joos et al. (2008) added the effect of the contribution of orographic waves to the vertical velocity. Penner et al. (2018) first used a wave spectrum (instead of a constant updraft velocity) together with the KL parameterization to treat the formation of ice crystals. They used the equatorial spectrum of observed gravity waves presented by Podglajen et al. (2016) together with the seasonal and latitudinal variations determined by Gary (2006, 2008). They also varied the standard deviation from Podglajen et al. (2016) based on the vertical stratification of atmospheric stability, atmospheric density, and topography. However, the radiative forcing of sulfate as well as all anthropogenic aerosols were not explored due to the deficiencies in the KL parameterization (Liu and Shi, 2018).

Secondary organic aerosols (SOAs) have been shown to have a highly viscous semisolid or even glassy state at low temperatures and low RH<sub>i</sub> in many experiments (Koop et al., 2011; Pajunoja et al., 2014; Renbaum-Wolff et al., 2013; Saukko et al., 2012). Observations also found SOA acting as INPs and in the ice crystal residues of cirrus clouds (Ignatius et al., 2016; Wagner et al., 2017; DeMott et al., 2003; Cziczko et al., 2013; Wilson et al., 2012). A peak in the number concentration of ultrafine particles was observed near 12 km in the Amazon and identified as primarily organic. Furthermore, a marker molecule indicated that a substantial fraction of the organics in aerosol-rich layers in the upper troposphere were associated with the oxidation of isoprene (Andreae et al., 2018). A modeling study that included the nucleation of new particles through organic nucleation predicted that there are a large number of accumulation mode SOA particles existing in the upper tropical troposphere which may be important for the ice nucleation (Zhu and Penner, 2019). SOA particles have a strong potential to act as INPs to form ice particles via heterogeneous freezing under the conditions conducive to ice formation in the upper troposphere (Knopf et al., 2018). However, the influence of SOA on cirrus clouds is not yet fully studied (but see Penner et al., 2018).

In this study, we combined the best features of the LP and KL parameterizations to develop a hybrid ice nucleation scheme that accounts for the changes in ice number concentrations in both the updrafts and downdrafts associated with a spectrum of gravity waves. Using a global climate model coupled with the new ice nucleation scheme, the radiative forcing of aircraft soot and sulfate was examined. Furthermore, the radiative forcing of anthropogenic aerosols on cirrus clouds since the PI time period was estimated both including and excluding the effect of changes in SOA. A global average negative anthropogenic forcing of  $-0.20 \pm 0.05 \text{ W m}^{-2}$  without SOA as a result of aerosol effects in cirrus clouds is suggested. The forcing is reduced to  $-0.04 \pm 0.08 \text{ W m}^{-2}$  when SOA is included.

## 2 Methodology

### 2.1 Model

We used the Community Earth System Model (CESM) version 1.2.2 (refer to <http://www.cesm.ucar.edu/models/cesm1.2/>, last access: 14 November 2019, for details) coupled to the University of Michigan IMPACT aerosol model (Liu et al., 2005, with updates as described herein) with a resolution of  $1.9^\circ$  (longitude)  $\times$   $2.5^\circ$  (latitude) and 30 vertical layers to simulate aerosols and their effects on cirrus clouds. This version of the IMPACT model simulates the number and mass of pure sulfate in three modes (i.e., nucleation,  $< 5 \text{ nm}$ ; Aitken,  $5\text{--}50 \text{ nm}$ ; and accumulation,  $> 50 \text{ nm}$ ) and their interaction with the following 14 other aerosol species/types. Sulfate is the only aerosol participating in homogeneous ice nucleation in the model. Soot from fossil fuel and biofuel burning (fSoot) is simulated in three modes with different hygroscopicities according to the number of monolayers of sulfate on its surface (Yun et al., 2013) while soot from biomass burning (bSoot) is simulated in one mode. a total of 0.05 % of fSoot with fewer than one monolayer of sulfate and 0.1 % of fSoot coated with one to three monolayers of sulfate as well as 0.1 % of bSoot are assumed to be effective INPs. The hygroscopicity of fSoot and bSoot is determined by volume averaging the hygroscopicity of the underlying particles and the number of sulfate monolayers on the particles. Aircraft soot is simulated in two modes. The first mode has acted as an ice nuclei within contrails that subsequently evaporated (cSoot). The second mode, which was not an ice nuclei within contrails, is not considered to act as an INP in the model. The soot that has already been included in contrail ice is pre-activated. We assume the pre-activated aircraft soot coated with fewer than three monolayers of sulfate to be an INP similar to the treatment in Zhou and Penner (2014) (see also Mahrt et al., 2019). Dust and sea salt are each carried in four separate bins with varying radii. Dust with fewer than three monolayers of sulfate coating is used to form heterogeneous INPs in the model. This treatment is consistent with the results of field studies by DeMott et al. (2003), Cziczko et al. (2004), and Richardson et al. (2007). The assumptions for aerosols to be effective INPs in the model are summarized in Table 1. The aerosols simulated by the IMPACT model are only able to nucleate the initial ice crystal number concentration in cirrus clouds in the CESM model. Thereafter, the growth and sedimentation as well as evaporation of ice crystals follow the treatment in the CESM. In addition, the changes to cirrus clouds have feedbacks as a result of changes to the radiation budget, temperature, and formation of warm clouds, as simulated in the CESM model.

### 2.2 Ice nucleation parameterization

The LP parameterization is only able to calculate the ice nucleation in a rising parcel, but it is not able to predict the

**Table 1.** Summary of assumptions for aerosols to be effective INPs in the model.

| Aerosol component     | Assumption to be effective INPs   |
|-----------------------|---|
| Fossil/bio-fuel OM–BC | 0.05 % of fSoot with fewer than one monolayer of sulfate and 0.1 % with one to three monolayers of sulfate when RH <sub>i</sub> reaches 120 %.  |
| Biomass OM–BC         | 0.1 % of bSoot when RH <sub>i</sub> reaches 120 %.  |
| Aircraft OM–BC        | Pre-activated aircraft soot within contrails with fewer than three monolayers of sulfate when RH <sub>i</sub> reaches 120 %.  |
| Dust                  | Dust with fewer than three monolayers of sulfate coating 120 % when RH <sub>i</sub> reaches.  |
| SOA                   | The newly formed SOA grows to the accumulation mode and meets the requirements of the glass transition temperature and RH <sub>i</sub> calculated using the equations in Wang et al. (2012) when RH <sub>i</sub> reaches 120 %. |

changes in the supersaturation or simulate the evaporation of ice in downdrafts. As a result, the scheme used by Penner et al. (2018) to treat gravity waves cannot be used with the LP parameterization as it was originally formulated. The KL scheme calculates the changes in the sub-grid-scale variation in RH<sub>i</sub> in a cloud parcel as a result of updrafts or downdrafts and the growth or decay of ice particles. Unlike some schemes (e.g., Shi et al., 2015) which consider that the initial nucleation in an updraft takes place in the presence of ice from the previous time step, we assume the first parcel updraft within a general circulation model (GCM) time step does not carry any preexisting ice. Thereafter if ice forms it may either grow and decrease the supersaturation or evaporate, adding water vapor to the parcel. However, aerosols freeze in the order of size bins and this neglects the competition among different aerosol size bins, which results in an underestimation of the ice formed from aerosols in small size bins and a low sensitivity to the change of aerosol number (Liu and Shi, 2018). In this study, we combined the LP and KL parameterizations to develop a new ice nucleation scheme (hereafter HYBRID) to make use of their strengths and avoid their defects.

In the HYBRID scheme, the supersaturation ( $S_i$ ) in the cloud parcel is calculated explicitly using the KL scheme so that ice particles are able to grow or decay throughout the time variations in the updrafts and downdrafts associated with gravity waves.  $S_i$  is calculated as a function of the updraft and aerosol concentrations at each grid.  $S_i$  is updated every second using

$$\frac{dS_i}{dt} = a_1 S_i w - (a_2 + a_3 S_i) \int_0^\infty dr_0 \frac{dn}{dr_0} R_{\text{im}}(r_0), \quad (1)$$

where the parameter  $a_1$  is given by  $a_1 = (L_s M_w g) / (c_p R T^2) - Mg / (RT)$ , with the molar mass of air  $M$  and water  $M_w$ , latent heat of sublimation  $L_s$ , constant of gravity  $g$ , heat capacity at constant pressure  $c_p$ , universal gas constant  $R$ , and air temperature  $T$ .  $w$  is the vertical velocity.  $a_2 = 1/n_{\text{sat}}$  with the water vapor number

density at ice saturation  $n_{\text{sat}}$ .  $a_3 = L_s^2 M_w m_w / (c_p p T M)$ , with the mass of a water molecule  $m_w$  and the air pressure  $p$ .  $R_{\text{im}}$  is the monodisperse freezing–growth integral,

$$R_{\text{im}} = \frac{4\pi}{v} \int_{-\infty}^t dt_0 \dot{n}_i(t_0) r_i^2(t_0, t) \frac{dr_i}{dt}(t_0, t), \quad (2)$$

where  $v$  is the specific volume of a water molecule.  $dt_0 \dot{n}_i(t_0)$  is the number density of aerosol particles that nucleate ice and freeze within the time interval between  $t_0$  and  $t_0 + dt_0$ ,  $r_i(t_0, t)$  is the radius of the spherical ice particle at time  $t$  that froze and commenced to grow at time  $t < t_0$ , and  $dr_i/dt$  is the radial growth rate of that ice particle. In the HYBRID scheme,  $\dot{n}_i(t_0)$  is determined using the LP parameterization.

A series of updraft velocities at each grid point were generated based on a fitted wave spectrum to the observed equatorial gravity waves from Podglajen et al. (2016). The standard deviation of this wave spectrum was extended to other latitudes and seasons by using the parameterization proposed by Gary (2006, 2008). It was extended vertically based on the static stability, atmospheric density, and topography. This parameterization of the wave spectrum associated with gravity waves is described in Penner et al. (2018).

When the updraft velocity is positive, the LP parameterization is used to calculate the increase in the ice number from homogeneous and/or heterogeneous freezing, so that the HYBRID scheme avoids the lack of sensitivity to changes in aerosol number in the KL parameterization when calculating the number of new ice particles. The LP parameterization is derived by fitting the results of a large set of parcel model simulations covering different conditions in the upper troposphere (Liu and Penner, 2005). Two separate regimes are identified by the sign of  $T - 6.07 \ln w + 55.0$  (where  $T$  is the temperature and  $w$  is the updraft velocity) to calculate the change of  $N_i$  due to homogeneous nucleation. When the sign is positive, the solution is in a fast-growth regime which is associated with higher  $T$  and lower  $w$ . The number concentration of new ice crystals ( $N_i$  or  $\dot{n}_i(t_0)$  as in the above) is



then calculated with the following equation:

$$N_i = \min \left\{ \exp(a_2) N_a^{a_1} \exp(bT) w^c, N_a \right\}, \quad (3)$$

where  $b = b_1 \ln N_a + b_2$ , and  $c = c_1 \ln N_a + c_2$ .  $N_a$  is the number concentration of sulfate in the Aitken and accumulation modes. The coefficients  $a_1$ ,  $a_2$ ,  $b_1$ ,  $b_2$ ,  $b_3$ ,  $c_1$ , and  $c_2$  are constant and can be found in Table 1 of Liu and Penner (2005). For lower  $T$  and higher  $w$  (the slow-growth regime), the following equation is applied to calculate  $N_i$ :

$$N_i = \min \left\{ \exp[a_2 + (b_2 + b_3 \ln w) T + c_2 \ln w] N_a^{a_1 + b_1 T + c_1 \ln w}, N_a \right\}, \quad (4)$$

where the coefficients  $a_1$ ,  $a_2$ ,  $a_3$ ,  $b_1$ ,  $b_2$ ,  $b_3$ ,  $c_1$ , and  $c_2$  are again listed in Table 1 of Liu and Penner (2005) and are different from those in the fast-growth regime. The number concentration of  $N_i$  from INPs in the heterogeneous nucleation regime is given as

$$N_i = \min \left\{ \exp(a_{22}) N_{\text{INP}}^{b_{22}} \exp(bT) w^c, N_{\text{INP}} \right\}, \quad (5)$$

where  $b = (a_{11} + b_{11} \ln N_{\text{INP}}) \ln w + (a_{12} + b_{12} \ln N_{\text{INP}})$  and  $c = a_{21} + b_{21} \ln N_{\text{INP}}$ .  $N_{\text{INP}}$  is the number concentration of total INPs. The coefficients  $a_{11}$ ,  $a_{12}$ ,  $a_{21}$ ,  $a_{22}$ ,  $b_{11}$ ,  $b_{12}$ ,  $b_{21}$ , and  $b_{22}$  can be found in Sect. 4.2 of Liu and Penner (2005). When the updraft velocity is low and temperature is high, heterogeneous ice nucleation takes place initially and depletes the water vapor in the parcel so that homogeneous ice freezing never occurs. The threshold temperature  $T_c$  for heterogeneous nucleation only is given by

$$T_c > a \ln(w) + b, \quad (6)$$

where  $a = -1.4938 \ln(N_{\text{INP}}) + 12.884$ ;  $b = -10.41 \ln(N_{\text{INP}}) - 67.69$ . When the regime is in a transition from heterogeneous-dominated to homogeneous-dominated regimes, the total ice number concentration from nucleation can be higher than the ice concentration from only heterogeneous nucleation but lower than that from the pure homogeneous nucleation case. Then,  $N_i$  is interpolated from

$$N_i = N_{\text{Het}} \left( \frac{N_{\text{Het}}}{N_{\text{Hom}}} \right)^{\frac{N_{\text{INP}} - N_c}{0.9 N_c}}, \quad (7)$$

where  $N_{\text{Het}}$  is the ice number from pure heterogeneous nucleation,  $N_{\text{Hom}}$  is the ice number from pure homogeneous nucleation,  $N_{\text{INP}}$  is the number concentration of INPs, and  $N_c$  is the critical number concentration of INPs for the heterogeneous nucleation-only regime.

Based on the method outlined above, the HYBRID scheme calculates the increase in  $N_i$  using LP parameterization. The new ice crystals from nucleation either grow or decay with consumption or evaporation of water vapor and therefore change  $S_i$ , which is determined using the KL parameterization. The changes in  $S_i$  then influence which particles are able to nucleate, forming ice crystals.

We define cirrus clouds for which the effects of aerosols are defined or calculated as all large-scale clouds formed at temperatures  $< -35^\circ$ . Cirrus clouds at these temperatures include anvil cirrus that are formed by the outflow from deep convection as well as large-scale cirrus formed by in situ gravity waves. The detrained ice crystal number concentration in anvils is calculated from the detrained ice mass by assuming a spherical particle with a constant volume-mean radius, which is approximated as  $3\rho_0 Q / (4\pi\rho_i r_{\text{iv}}^3)$  following Lohmann (2002).  $\rho_i$  is the ice crystal density,  $\rho_0$  is the air density,  $r_{\text{iv}}$  is the volume mean radius determined from a temperature-dependent lookup table (Kristjánsson et al., 2000; Boville et al., 2006), and  $Q$  is the detrainment rate of cloud water mass diagnosed from the convection parameterization. The new clouds generated by convective detrainment are assumed to be at saturation with respect to ice. In doing this, anvil clouds and in situ cirrus compete for the available water vapor within a grid box. When anvil clouds are formed due to convective detrainment, it reduces the saturation ratio in the clear-sky portion of a grid and can potentially reduce the frequency of in situ large-scale cirrus formation (Wang and Penner, 2010; Wang et al., 2014). We only calculate  $N_i$  as a result of the nucleation of aerosol in large-scale cirrus, so that when anvils occur in a grid box, we average the concentrations to determine the total ice number concentration in cirrus clouds. Anthropogenic emissions contribute to the change in the number concentration of ice crystals in large-scale cirrus cloud, but these are then averaged with the crystals in anvils.

### Evaluation of the HYBRID scheme

In order to examine the ability of the HYBRID ice nucleation scheme to simulate ice number concentration, the results from a box model using the HYBRID scheme are compared with those from an adiabatic parcel model under the same simulation conditions. The adiabatic parcel model was that used to generate the LP parameterization and was introduced in Liu and Penner (2005). The two models are run for 30 min for each simulation, which is the time step used in the CESM. During the 30 min, the updraft velocity is updated every 2.2 min as recommended by Podglajen et al. (2016). The ice number concentrations after the 30 min simulation from the two models are compared. We ran both the adiabatic parcel model and the HYBRID box model using a constant updraft velocity for each 2.2 min interval. When the velocity is positive ice crystals form and grow in the HYBRID box model as described above. For downdrafts, if the supersaturation is below 100 %, the two models use the same method to simulate the evaporation of any existing ice particles, which is also the same method used in the global model as suggested in Kärcher et al. (2006). The scheme used here for the HYBRID box model is the same as the HYBRID scheme used in the global model. Note that the final interval within each 30 min simulation is shortened in order to match the

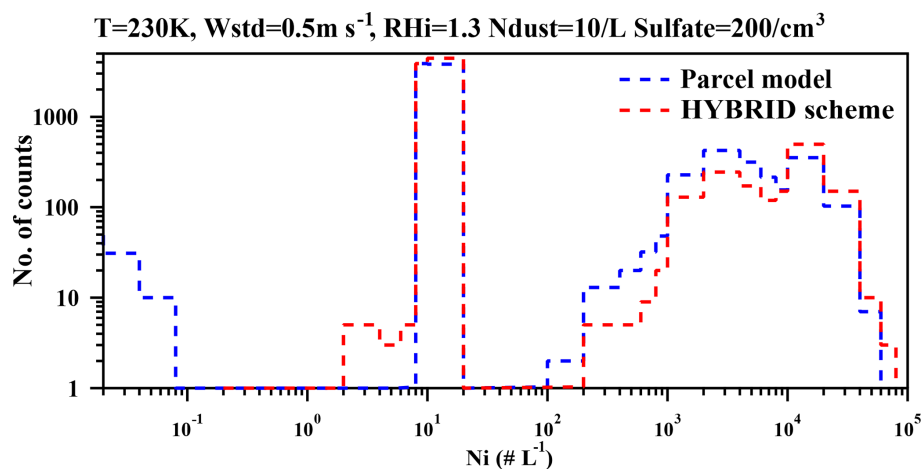


**Figure 1.** Histogram of predicted ice number concentration for 10 000 simulations using an adiabatic parcel model (blue dashed line) and a box model using the HYBRID scheme (red dashed line). Wstd is the standard deviation of the assumed pdf of updraft velocities, while Ndust and Sulfate are the assumed dust and sulfate number concentrations.

treatment used in the CESM/IMPACT model which uses a 30 min time step. When run within the CESM model, this final ice number concentration is then passed back to the CESM model after this 30 min interval.

The updraft- and downdraft-associated gravity waves are determined from a Laplace distribution as suggested by the fit to the observed gravity waves by Podglajen et al. (2016). We conducted 10 000 simulations using a random selection of the updrafts and downdrafts for each model. Both models use the same selection of updrafts and downdrafts in each simulation. We set up an initial condition with a temperature of 230 K, the standard deviation for the updraft velocities was  $0.5 \text{ m s}^{-1}$ , and the initial RH<sub>i</sub> was 130 %. The sulfate number concentration was set to  $0.2 \text{ L}^{-1}$  while the dust concentration was  $10 \text{ L}^{-1}$ . These particles then participate in either homogeneous nucleation or heterogeneous immersion nucleation.

Figure 1 shows a histogram of the predicted ice number concentration ( $N_i$ ) for 10 000 simulations of the adiabatic parcel model and the box model using the HYBRID scheme. Two populations of  $N_i$  are shown in Fig. 1. The lower population (with concentrations of the order of  $10 \text{ L}^{-1}$  or less) represents primarily heterogeneous nucleation on dust particles, while the higher population (with concentrations of the order of  $10^2 \text{ L}^{-1}$  or more) represents primarily homogeneous nucleation on sulfate aerosols. The results in the simulations dominated by heterogeneous nucleation are mostly similar for the two models, although the HYBRID scheme overestimates the  $N_i$  between 1 and  $10 \text{ L}^{-1}$  when the results from the adiabatic parcel model are less than  $10^{-1} \text{ L}^{-1}$  for some of these same simulations. The average  $N_i$  from heterogeneous nucleation over 10 000 simulations from the adiabatic parcel model is  $9.40 \pm 2.31 \text{ L}^{-1}$ , while that from the HYBRID scheme is  $9.52 \pm 2.08 \text{ L}^{-1}$ .

The box model using the HYBRID scheme predicts larger  $N_i$  from homogeneous nucleation than the parcel model in

the 88 % of simulations where homogeneous nucleation occurs. There are more simulations using the HYBRID scheme that predict larger  $N_i$  from homogeneous nucleation than the parcel model as indicated by a larger number of counts of large  $N_i$  ( $10^4 \text{ L}^{-1}$  or more) in Fig. 1. The HYBRID scheme uses the LP parameterization for every small time step of 2.2 min. Since the LP parameterization was built using the largest  $N_i$  in an ascending parcel after 30 min, there is a tendency for the HYBRID scheme to overpredict  $N_i$ . The average  $N_i$  from homogeneous nucleation over the 10 000 simulations in the two models is  $1.41 \pm 4.23 \text{ L}^{-1}$  from the parcel model, while it is  $1.52 \pm 4.83 \text{ L}^{-1}$  from the HYBRID model. The HYBRID scheme overestimates the  $N_i$  from homogeneous nucleation by 7.4 %, which dominates the difference in total  $N_i$  between two models. Overall, the average total  $N_i$  over the 10 000 simulations is  $1.53 \pm 4.83 \text{ L}^{-1}$  using the HYBRID scheme, which is 7.3 % larger than the result from the parcel model ( $1.42 \pm 4.23 \text{ L}^{-1}$ ). We also examined the difference between the above case when sulfate was  $200 \text{ cm}^{-3}$  compared to when sulfate was  $20 \text{ cm}^{-3}$ , and the difference was within 7.2 % of that using the full parcel model. Although the HYBRID scheme predicts a somewhat larger number of nucleated ice particles, on average, the results are reasonable compared to the results from the parcel model.

### 2.3 Experiments with the global model

We performed a series of model experiments in which different emissions of aerosols and aerosol precursors are used. Table 2 provides a summary of these experiments. The base case (PD\_Base) uses emissions for the present day (PD, for the year 2000) for anthropogenic sulfur and soot from fossil fuel adopted from the Community Emission Data System (CEDS) (Hoesly et al., 2018). Emissions from van Marle et

**Table 2.** Description of cases.

| Case name | Description   |
|-----------|---|
| PD_Base   | Emissions for the present day ( $\approx 2000$ ) for anthropogenic sulfur and surface and aircraft soot   |
| PI_cSoot  | As in PD_Base without INPs from pre-activated aircraft soot in contrails  |
| PI_SO4    | As in PD_Base, but with the anthropogenic sulfur emission for the preindustrial period ( $\approx 1750$ CE)   |
| PI_ALL    | As in PD_Base, but with the anthropogenic sulfur emission and surface soot emission for the preindustrial period ( $\approx 1750$ CE) and without aircraft soot |
| PD_SOA    | As in PD_Base, but adding INPs from newly formed SOA particles in the present day   |
| PI_SOA    | As in PI_ALL, but adding INPs from newly formed SOA particles in the preindustrial period   |

Note: SOA: secondary organic aerosol; INP: ice-nucleating particle.

al. (2017) are adopted for biomass burning emissions. These emissions are the same as the emissions data sets used for the CMIP6 simulations. The year 2000 emissions are used for all years of our simulation. We included soot from aircraft for 2006 based on the Aviation Environment Design Tool (AEDT) data set (Barrett et al., 2010). The AEDT data are presumed to be more accurate than the CMIP6 aircraft emissions since they were developed based on the original flight tracks of each of 31 million commercial flights worldwide (Wilkerson et al., 2010). The dimethylsulfide (DMS) emissions from the ocean are assumed constant in the PD and PI periods (Tilmes et al., 2016). The emission of dust uses the scheme from Zender et al. (2003). In a sensitivity experiment (PI\_cSoot), the emission of cSoot is removed from PD\_Base to examine its impact on ice number concentration and radiative forcing. We also set a case (PI\_SO4) with the emission of anthropogenic sulfur changed to PI ( $\approx 1750$ ) to calculate the radiative forcing of sulfur. The case PI\_ALL set all emissions to those of the PI period ( $\approx 1750$ ) to examine the radiative forcing of all anthropogenic aerosols on cirrus cloud. Additionally, we set up two experiments to examine the effect of SOA as an INP on anthropogenic forcing in cirrus clouds. The cases PD\_SOA and PI\_SOA add newly nucleated SOA particles that have grown to the accumulation mode as additional INPs to the cases of PD\_Base and PI\_ALL. The cases including SOA in the PD and PI read in the explicit number concentration of newly formed SOA in the accumulation mode nucleated from highly oxygenated organic molecules (HOMs) that form from the oxidation of  $\alpha$ -pinene. The nucleated SOA particles grow by deposition and coagulation of sulfuric acid as well as the oxidation products of isoprene,  $\alpha$ -pinene, limonene, and aromatics, which are in the aerosol phase. This SOA was simulated using the version of the

CESM/IMPACT model outlined in Zhu et al. (2017, 2019) and Zhu and Penner (2019, 2020). The SOA that meets the requirements of the glass transition temperature and  $RH_i$  calculated using the equations in Wang et al. (2012) acts as an effective heterogeneous INP.

The changes in aerosol emissions only influence the number concentration of ice nuclei in the CESM and thereby give the indirect radiative effect in cirrus clouds. The direct radiative effect caused by the change of aerosols is not included. Clear-sky radiative forcing in this study is not associated with direct aerosol radiative forcing but is rather mainly due to changes in water vapor which leads to changes in the clear-sky longwave radiation (Wang and Penner, 2010). All cases were run with prescribed sea surface temperatures for the present day, and winds were nudged towards ECMWF re-analysis data for the years 2005–2011 using a nudging time of 6 h (Zhang et al., 2014). The data for the last 6 years were used for analysis in this study.

### 3 Results from the global model

#### 3.1 Ice number concentrations

The predicted  $N_i$  in the PD\_Base case is compared with the observed  $N_i$  reported by Krämer et al. (2009, 2020) in Fig. S1 in the Supplement. Data from the model have been selected to have ice water mixing ratios  $> 10^{-8}$  kg kg $^{-1}$  to match values seen in the in situ observations (Krämer et al., 2016). The global model using the HYBRID scheme is able to do a reasonable job in predicting  $N_i$  with the difference in the median value between the simulation and observation less than 50 % for all temperatures except for the high concentrations seen between 197 and 213 K. The model predicts  $\sim 3$  times higher  $N_i$  on average compared to the observations between 197 and 213 K. Although the comparison of ice number concentration between our model and observation has not improved significantly compared to that shown by Penner et al. (2018), the new nucleation scheme improves the ability of nucleation to occur on small-sized particles, since it avoids the calculation of ice nucleation chronologically from large sizes to small sizes used in the KL scheme, which results in an underestimation of ice crystals formed from small-sized particles.

The global average  $N_i$  in the PD\_Base is  $0.15 \times 10^{10}$  m $^{-2}$  with the largest  $N_i$  in the tropics of the eastern hemisphere (Fig. 2a). Most ice particles nucleate in the upper troposphere (150–200 hPa) in the tropics, while some ice nucleation occurs in the lower troposphere (around 300 hPa) in the polar regions (Fig. 2b). The ice particles formed from homogeneous nucleation dominate the total  $N_i$  in most regions over the world (Fig. S2a) and are responsible for  $\sim 95$  % of global average  $N_i$  (Fig. 2c). The large number concentration of sulfate in the Aitken and accumulation modes in the upper troposphere over the west Pacific Ocean and north Indian Ocean contributes to the remarkably large  $N_i$  in the tropical east-

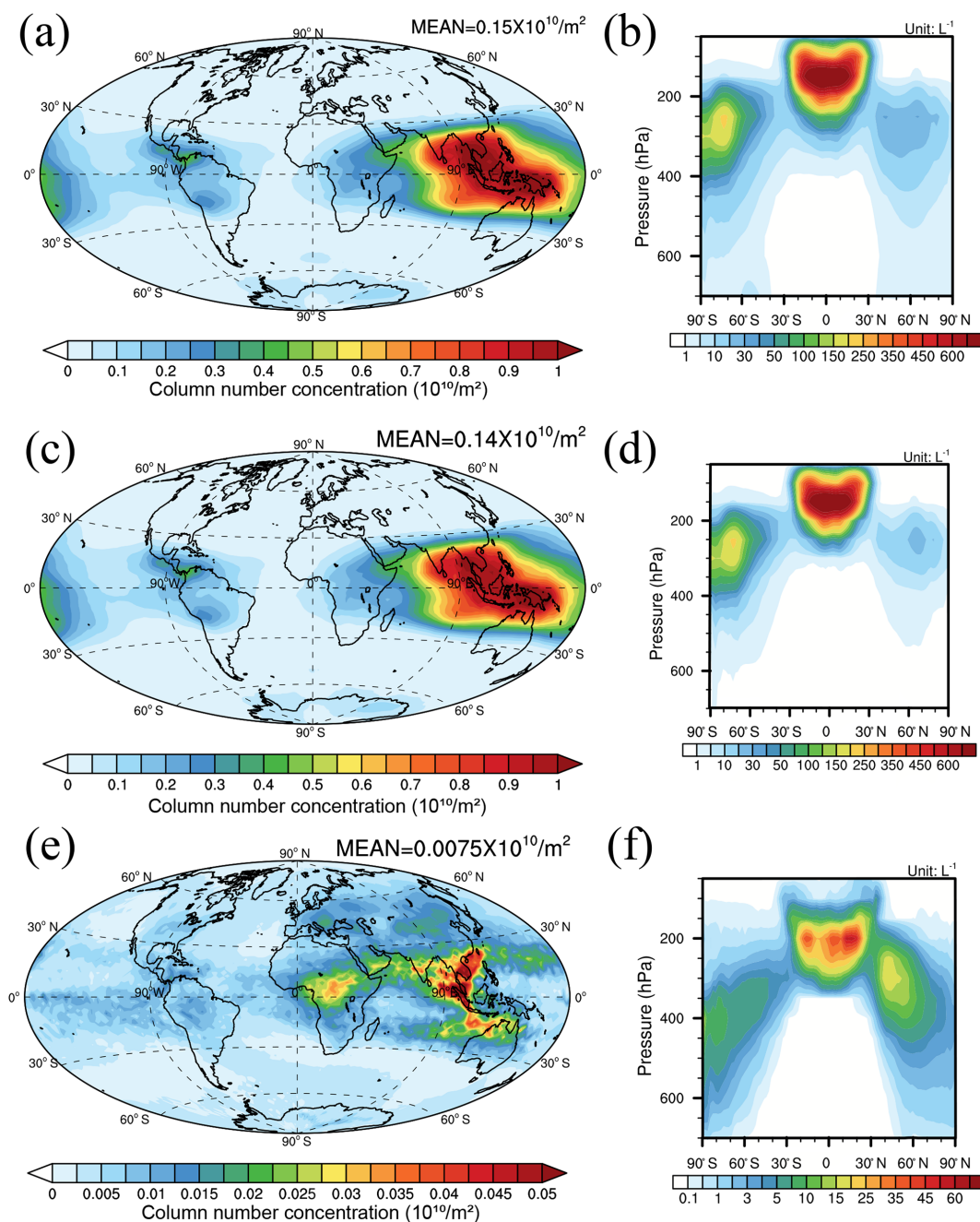


**Figure 2.** The vertically integrated total  $N_i$  in the PD\_Base case (a),  $N_i$  from homogeneous nucleation (c), and  $N_i$  from heterogeneous nucleation (e). The zonal average plots of  $N_i$  in the PD\_Base case (b),  $N_i$  from homogeneous nucleation (d), and  $N_i$  from heterogeneous nucleation (f). Note: the vertical axes in (b), (d), and (f) are in hybrid pressure levels.

ern hemisphere. Heterogeneous nucleation dominates the  $N_i$  in the northern middle–high latitudes where anthropogenic soot emission is high (Fig. S2a), although the  $N_i$  from heterogeneous nucleation is high in the tropics (Fig. 2e). Homogeneous nucleation mostly occurs in the upper troposphere (around 200 hPa in the tropics and around 300 hPa in the extratropical regions), while heterogeneous nucleation is an important contributor to  $N_i$  in the middle and lower troposphere

(Fig. S2b). Although the  $N_i$  from homogeneous nucleation is high, the occurrence frequency of homogeneous nucleation (calculated as the ratio of the time steps when homogeneous nucleation occurs to all time steps with nucleation occurring) is up to  $\sim 20\%$  in the tropics and  $< 5\%$  in most other regions (Fig. S2c). Due to the lack of the effect of orographic waves on ice nucleation, the observed increases in ice number over

orography, particularly over the Andes, Rockies, Antarctic mountains, and Greenland, are not shown in Fig. 2.

The competition between the heterogeneous INPs and homogeneous haze particles determines the change in  $N_i$  between the PD and PI periods. We set up three sensitivity cases to separately examine the effects of the emission of cSoot for aircraft, anthropogenic sulfur, and all anthropogenic emissions on  $N_i$ . INPs always nucleate prior to homogeneous nucleation in a rising air parcel, so they consume the available water vapor and inhibit homogeneous freezing when added to regions dominated by homogeneous nucleation. The  $N_i$  formed from heterogeneous nucleation increases significantly around 200 hPa over the world due to the inclusion of INPs from cSoot, especially near Southeast Asia (Fig. 3e, f). Simultaneously, homogeneous nucleation is inhibited significantly around 200 hPa in Southeast Asia and other tropical regions (Fig. 3c, d). The emissions of aircraft soot that form contrails peak near 200 hPa with the spatial distribution shown in Fig. 1a in Zhou and Penner (2014). Although the emissions of aircraft soot are large in the midlatitudes, the effect of inhibiting homogeneous nucleation as a result of adding the heterogeneous nucleation is large in the tropics (Fig. 3c). That is because of the largest number concentration of ice nuclei from homogeneous nucleation in the tropics as shown in Fig. 2c. Due to the much larger decrease in  $N_i$  from homogeneous nucleation than the increase in  $N_i$  from heterogeneous nucleation, the global average  $N_i$  is decreased by  $0.1 \times 10^8 \text{ m}^{-2}$  (1 %) when including the emission of aircraft soot (Fig. 3a). The change in  $N_i$  due to cSoot is small with a significant change only over the North Atlantic Ocean and east coastal regions in North America (Fig. 3a).

In contrast to the case of aircraft soot, the increase in the sulfur emissions from PI to PD leads to a large increase in  $N_i$  from homogeneous nucleation in most regions, which causes an increase of  $1.01 \times 10^8 \text{ m}^{-2}$  in the global average  $N_i$  (Fig. 4c). The increase in  $N_i$  from homogeneous nucleation contributes to the significant increase in  $N_i$  near 150 hPa over South Asia, Africa, and the north Indian Ocean (Fig. 4a). The decrease in  $N_i$  from heterogeneous nucleation offsets some of the increase in  $N_i$  from homogeneous nucleation and leads to a significant decrease in  $N_i$  near 300 hPa over the North Pacific Ocean (Fig. 4a). In total, the global average  $N_i$  is increased by  $0.73 \times 10^8 \text{ m}^{-2}$  (5 %) due to the increase in sulfur emissions.

The change in  $N_i$  from PI to PD due to all anthropogenic emissions is a balance among the effects of increasing INPs from surface emissions and aircraft soot as well as the increase in haze particles. The effect of all anthropogenic emissions on  $N_i$  is mostly dominated by the increase in  $N_i$  from homogeneous nucleation caused by the increase in sulfur emissions, but homogeneous nucleation is inhibited somewhat by increased INPs from soot (compare Figs. 5c and 4c). As a result, the global average increase in  $N_i$  from homogeneous nucleation between PD\_Base and PI\_ALL is only 58 % of that between PD\_Base and PI\_SO4. The change

in  $N_i$  from heterogeneous nucleation is decreased in the midlatitudes to high latitudes of the Northern Hemisphere (NH) from PD\_Base to PI\_ALL similar to the decrease from PD\_Base to PI\_SO4 (Fig. 5e, f). However, the increase in INPs from soot near Southeast Asia leads to a small increase in  $N_i$  from heterogeneous nucleation there (Fig. 5e). In total, the increase in all anthropogenic emissions causes a significant increase in  $N_i$  in South Asia and the north Indian Ocean while a significant decrease in  $N_i$  is found in midlatitude regions and some Arctic regions, resulting in  $0.49 \times 10^8 \text{ m}^{-2}$  (3 %) more  $N_i$  from PI to PD for the global average.

It is conspicuous that sulfur and aircraft soot emissions have effects with different signs for the change in  $N_i$  (Figs. 3a, 4a). Generally, INPs from aircraft soot decrease  $N_i$  due to the suppression of homogeneous nucleation in the regions dominated by homogeneous nucleation, while the increase in sulfur emissions increases  $N_i$  in these same regions due to the enhancement of homogeneous nucleation. However, the changes to  $N_i$  have opposite signs in the west Pacific Ocean off the coast of Southeast Asia, where the homogeneous nucleation is most active (Fig. 2c). We attribute this to the possible effect of aerosol and cloud feedbacks to the meteorological state. When including aircraft soot, the temperature is decreased (Fig. S3b) and the RH<sub>i</sub> is increased (Fig. S3a) around 150 hPa over the west Pacific Ocean, where  $N_i$  from homogeneous nucleation increases a lot (Fig. 3c). The decrease in temperature is beneficial to homogeneous nucleation. Meanwhile, the emission of aircraft soot is very low in the west Pacific Ocean due to the lack of flight routes there (refer to Fig. 1a in Zhou and Penner, 2014), so that the effect of aircraft soot on the suppression of homogeneous nucleation is weak in that region (Fig. 3e). As a result, the  $N_i$  from homogeneous nucleation is increased, which determines the increase in the  $N_i$  near 150 hPa over the west Pacific Ocean due to the emission of aircraft soot (Fig. 3a). Similarly, when the sulfur emissions are increased from PI to PD, the change in cirrus clouds influences the meteorological state. A large decrease in RH<sub>i</sub> at 150 hPa is found in the west Pacific Ocean (Fig. S4a), so that the occurrence frequency of homogeneous nucleation decreases when sulfur emissions increase (Fig. S4d). Additionally, the temperature at 150 hPa increases over the world (Fig. S4b), which also contributes partly to the decrease in the occurrence frequency of homogeneous nucleation. Although global sulfur emissions increase sharply from PI ( $2.2 \text{ Tg S yr}^{-1}$ ) to PD ( $55 \text{ Tg S yr}^{-1}$ ), the anthropogenic emissions mainly occur on the mainland with much smaller emissions over the ocean even though the sulfur emissions from shipping increase by  $6.4 \text{ Tg S yr}^{-1}$ . The column number concentration of sulfate having the potential to freeze homogeneously does not increase significantly over most ocean regions (Fig. S4c), so that the decrease in the occurrence frequency of homogeneous nucleation leads to a decrease in  $N_i$  from homogeneous nucleation over the west Pacific Ocean (Fig. 4c). The increase in the temperature in the upper troposphere over the world

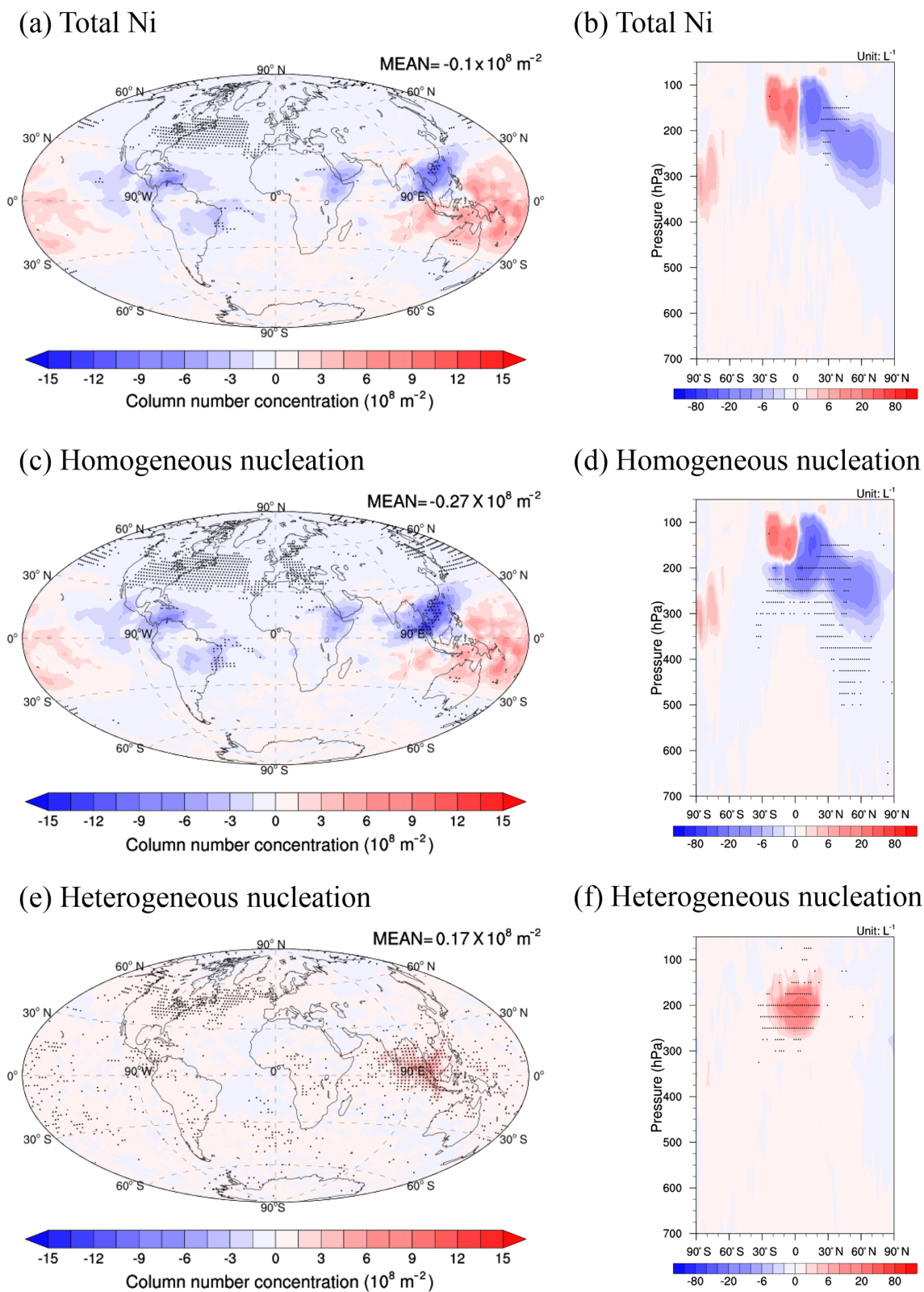
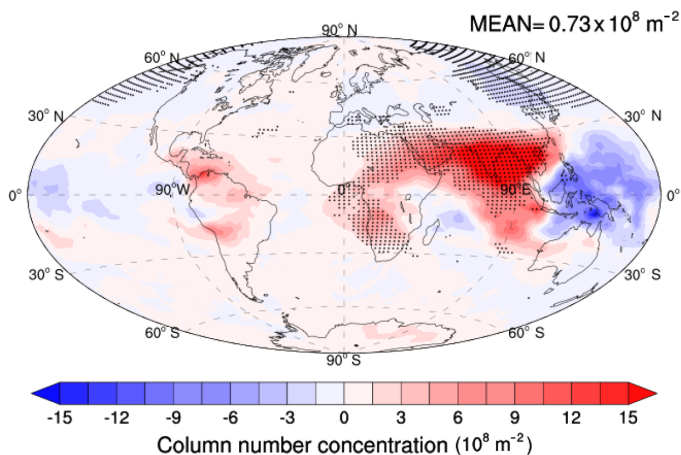


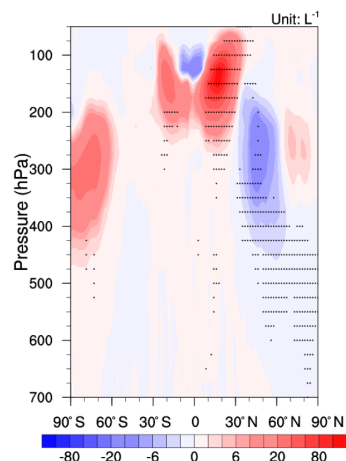
**Figure 3.** The annual average change in column number concentration (a, c, e) and zonal average number concentration (b, d, f) of total ice (a, b), ice from homogeneous nucleation (c, d), and ice from heterogeneous nucleation (e, f) for the difference between the PD\_Base and PI\_cSoot cases. Differences significant at the 90 % level according to a Student's *t* test are depicted by points.



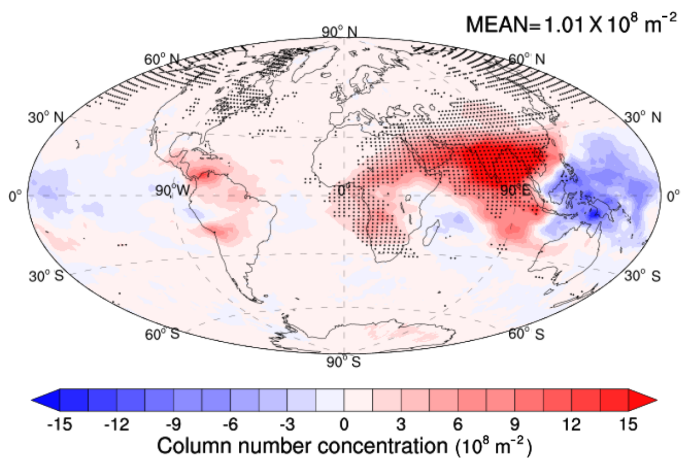
(a) Total Ni



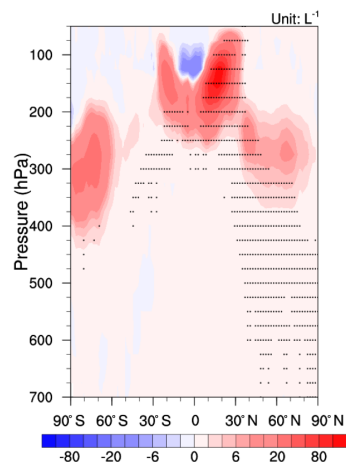
(b) Total Ni



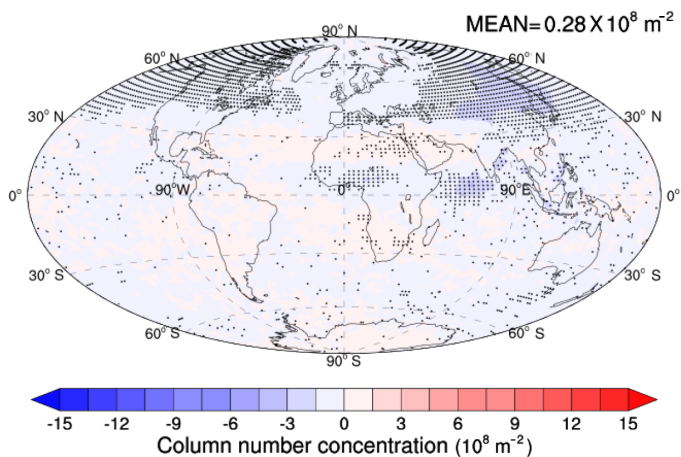
(c) Homogeneous nucleation



(d) Homogeneous nucleation



(e) Heterogeneous nucleation



(f) Heterogeneous nucleation

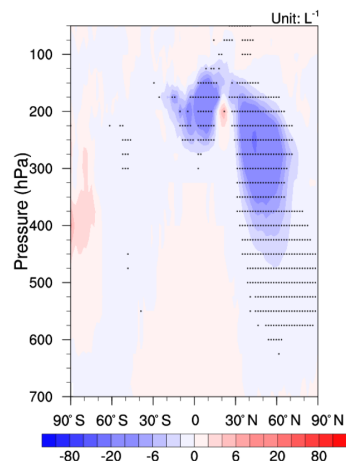


**Figure 4.** As in Fig. 3 but for the difference between the PD\_Base and PI\_SO4 cases. Differences significant at the 90% level according to a Student's *t* test are depicted by points.



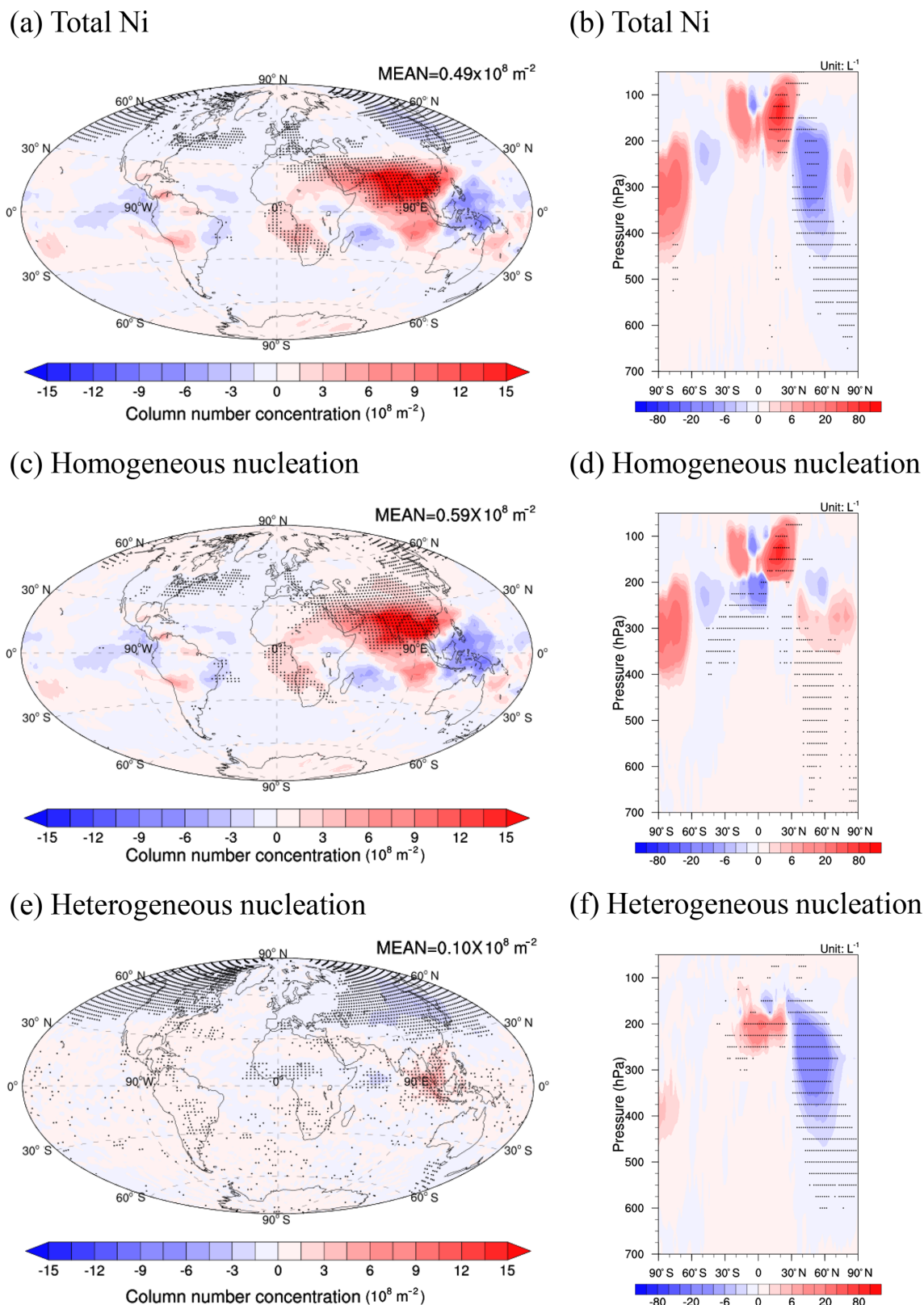


**Figure 5.** As in Fig. 3 but for the difference between the PD\_Base and PI\_ALL cases. Differences significant at the 90 % level according to a Student's *t* test are depicted by points.

(Fig. S4b) also partly explains the decrease in  $N_i$  from heterogeneous nucleation when only sulfur emissions increase (Fig. 4e). The feedbacks to the meteorological state in remote regions always have an opposite effect on the changes in  $N_i$  compared to the effect in regions with large anthropogenic emissions. These meteorological feedbacks partly reduce the changes in global average  $N_i$  due to anthropogenic emissions. Although these opposite changes in  $N_i$  due to meteorological feedbacks are not statistically significant (Figs. 3a, 4a, 5a), our conjecture based on the model results indicates that the meteorological feedbacks caused by the radiative effects of aerosols might contribute to the change in  $N_i$  in remote regions. These important feedback processes need to be investigated further.

### 3.2 Radiative forcing

The decrease in  $N_i$  in the upper troposphere usually leads to an increase in the size of ice particles, which promotes the gravitational removal and formation of snow, causing a decrease in the ice water path (IWP) and vice versa. As a result, the change in IWP is mainly determined by the change in  $N_i$  and has a similar geographic pattern. The global average IWP in the model is  $14.6 \text{ g m}^{-2}$  for the PD\_Base case, which is lower than that observed in different CloudSat and CALIPSO analyses ( $21\text{--}28 \text{ g m}^{-2}$ ) (Li et al., 2012). We used a cutoff diameter of  $250 \mu\text{m}$  to move cloud ice to snow. A cutoff diameter of  $400 \mu\text{m}$  in the model almost doubles the IWP in our model (compare IWP of dbfc\_mg10 and dbfc in Table 3 in Penner et al., 2018). The emission of aircraft soot leads to a significant decrease in IWP in Southeast Asia and the east coast of North America, caused by the inhibition of homogeneous nucleation (Fig. 6a). As shown in Fig. 6b, the increase in the sulfur emissions leads to a significant increase in IWP in the north Indian Ocean due to the changes in  $N_i$  from homogeneous nucleation. The decrease in IWP in East Asia and the Arctic is attributed to the decrease in  $N_i$  from heterogeneous nucleation (Fig. 6b). The geographic pattern of changes in IWP due to the change in all anthropogenic emissions from PI to PD is dominated by the changes in IWP caused by the changes in sulfur emissions (compare Fig. 6b and c). However, the increase in IWP in tropical regions is smaller, and the decrease in IWP in the middle and high latitudes of the NH is more negative in the PD\_Base-PI\_ALL case compared to the PD\_Base-PI\_SO4 case because of the inhibition of homogeneous nucleation caused by the increase in the emission of surface and aircraft soot. As a result, although the geographical pattern of the changes in IWP is similar for the PD\_Base-PI\_ALL and PD\_Base-PI\_SO4 cases, the magnitude of changes in the global average IWP switches from positive ( $0.07 \text{ g m}^{-2}$  for PD\_Base-PI\_SO4, Fig. 6b) to negative ( $-0.13 \text{ g m}^{-2}$  for PD\_Base-PI\_ALL, Fig. 6c).

The changes in  $N_i$  and IWP lead to a change in the cirrus cloud fraction and also feedback to produce a change in the lapse rate of temperature, which has an effect on the

delivery of water vapor and the strength of convection, and these changes influence the formation and lifetime of liquid water clouds. The liquid water path (LWP) changes due to these complex dynamical feedbacks are shown in Fig. S5. The changes in global average LWP are all less than 0.5 % with only a small number of grids with a significant change. The changes in the shortwave and longwave radiative fluxes are determined by the changes in LWP and IWP (as well as the change in  $N_i$ ), although they are dominated by the change in IWP. The changes in aerosol only have a direct effect on the cirrus clouds in our model, while the changes in warm clouds are caused by feedbacks due to the change in cirrus clouds. The changes in the all-sky shortwave radiative forcing (SRF) and longwave radiative forcing (LRF) at the top of the atmosphere (TOA) generally follow the changes in IWP but have the opposite sign (Figs. 7, 8, and 9). The changes in LWP could either enhance or offset the effect of changes in IWP on the radiative fluxes depending on whether the sign of the changes in IWP and LWP reinforces or not. The emission of cSoot leads to a positive global average SRF due to the significant increase in shortwave radiative fluxes off the coast of East Asia and over the north Indian Ocean, while the significant decrease in the longwave radiative fluxes over East Asia, the north Indian Ocean, and North Atlantic Ocean contribute to a negative global average LRF mostly due to the decrease in the global average IWP (Fig. 7). On the other hand, the increase in sulfur emissions causes a negative global average SRF largely due to the significant decrease over South Asia, North Africa, and the north Indian Ocean (Fig. 8a). Simultaneously, the increase in the IWP in these regions leads to a significant increase in longwave radiative fluxes resulting in a positive global average LRF, although the LRF is significantly negative in the middle to high latitudes over the east coast of Asia (Fig. 8b). The changes in the SRF and LRF due to the increase in all anthropogenic emissions have a similar geographic pattern to those caused by the increase in sulfur emissions but the global average forcings have opposite signs (compare Figs. 8c, d and 9c, d). This is due to the decrease in the global average IWP caused by the inhibition of homogeneous nucleation as a result of the increased emissions of soot.

The total all-sky net forcing (NRF) is determined by the balance between SRF and LRF. The radiative effects in cirrus clouds are dominated by longwave radiative effects. However, it is still possible that the radiative forcing due to changes in  $N_i$  in cirrus clouds in some regions is dominated by SRF due to the combined effects on shortwave forcing from the changes in cirrus clouds together with changes to warm clouds caused by feedbacks. The emission of cSoot has a negative global average NRF of  $-0.14 \pm 0.07 \text{ W m}^{-2}$  in cirrus clouds with only a few significant grids, although the SRF and LRF due to cSoot are significant in some coastal regions off of East and South Asia (Fig. 7). The NRF due to cSoot is most negative around  $30^\circ \text{ N}$  where the emission of aircraft soot is high, while there is a small positive forcing around

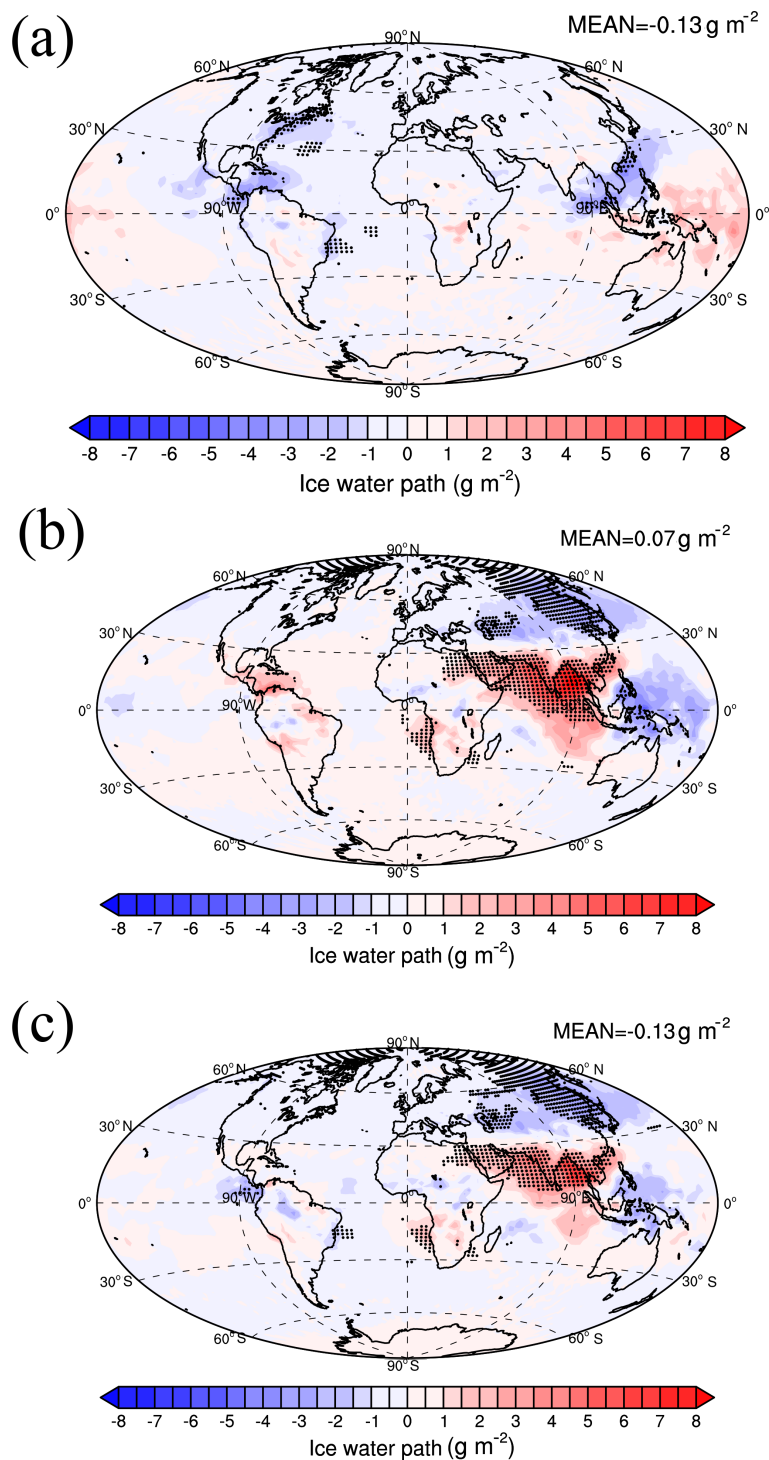


**Figure 6.** Annual mean plots of the change in vertically integrated averaged ice water path for the difference between the PD\_Base and PI\_cSoot cases (a), PD\_Base and PI\_SO4 cases (b), and PD\_Base and PI\_ALL cases (c). Differences significant at the 90 % level according to a Student's  $t$  test are depicted by points.

**Table 3.** Forcing and cloud changes associated with changes in aircraft soot, sulfur, and all anthropogenic aerosols.

| Parameter                       | PD_Base-PI_cSoot | PD_Base-PI_SO4   | PD_Base-PI_ALL   | PD_SO4-PI_SO4    |
|---------------------------------|------------------|------------------|------------------|------------------|
| $N_i$ ( $10^7 \text{ m}^{-2}$ ) | $-1.00 \pm 2.40$ | $7.26 \pm 2.88$  | $4.93 \pm 1.80$  | $11.96 \pm 2.29$ |
| IWP ( $\text{g m}^{-2}$ )       | $-0.13 \pm 0.06$ | $0.07 \pm 0.06$  | $-0.13 \pm 0.04$ | $-0.12 \pm 0.05$ |
| LWP ( $\text{g m}^{-2}$ )       | $-0.19 \pm 0.04$ | $0.16 \pm 0.07$  | $-0.05 \pm 0.08$ | $0.03 \pm 0.06$  |
| SRF ( $\text{W m}^{-2}$ )       | $0.35 \pm 0.13$  | $-0.36 \pm 0.10$ | $0.10 \pm 0.06$  | $-0.14 \pm 0.11$ |
| LRF ( $\text{W m}^{-2}$ )       | $-0.49 \pm 0.09$ | $0.33 \pm 0.05$  | $-0.30 \pm 0.06$ | $0.10 \pm 0.04$  |
| NRF ( $\text{W m}^{-2}$ )       | $-0.14 \pm 0.07$ | $-0.02 \pm 0.06$ | $-0.20 \pm 0.05$ | $-0.04 \pm 0.08$ |

Note: Differences significant at the 90 % level according to a Student's  $t$  test are italic.

$10^\circ \text{ N}$  dominated by SRF (Fig. 7f). The NRF is the sum of the clear-sky net radiative forcing (NRFC) and the cloud radiative forcing (CRF) caused by changes in cSoot. The global average CRF is  $-0.10 \pm 0.07 \text{ W m}^{-2}$ , which dominates over the NRFC and explains 72 % of the NRF of cSoot (Fig. 7c, d).

Although the increase in sulfur emissions from PI to PD leads to an increase in the global average  $N_i$  and IWP, the global average NRF due to sulfur emissions is near zero,  $-0.02 \pm 0.06 \text{ W m}^{-2}$ . The NRF due to sulfur emissions is significant and positive (up to  $7.1 \text{ W m}^{-2}$ ) around  $30^\circ \text{ N}$  in South Asia and North Africa (Fig. 8e). The NRF is negative over most middle to high latitudes of the NH, which is attributed to the decrease in LRF associated with the feedback to the decrease in  $N_i$  from heterogeneous nucleation there. However, the significant negative NRF in the north Indian Ocean and positive NRF in the west Pacific Ocean are dominated by the change in SRF (Fig. 8a, e). The LWP increases in the north Indian Ocean as a result of dynamic feedbacks from the changes in the cirrus clouds, leading to the significant SRF together with the changes in IWP and cirrus clouds. The negative NRF in the north Indian Ocean and middle to high latitudes of the NH offset the positive NRF around  $30^\circ \text{ N}$  (Fig. 8e). The significant negative NRF over the north Indian Ocean is dominated by the CRF, while the significant positive NRF over South Asia and North Africa is the combined effect of CRF and NRFC. The global average CRF is  $-0.17 \pm 0.06 \text{ W m}^{-2}$  and determines the sign of the global average NRF. However, the global average NRFC is  $0.14 \pm 0.02 \text{ W m}^{-2}$  with a wide area of positive values over the NH, which offsets most of CRF.

Compared to the NRF due to the increased sulfur emissions, the NRF is less positive in South Asia and more negative over the middle to high latitudes of the NH and the north Indian Ocean when including the increased emissions of surface and aircraft soot as well as sulfur together (Fig. 9e). In the middle to high latitudes of the Southern Hemisphere (SH), SRF and LRF always cancel each other so that NRF is negligible. As a result, the global average NRF due to all the increased anthropogenic emissions from PI to PD is  $-0.20 \pm 0.05 \text{ W m}^{-2}$ , which is mainly dominated by the changes in LRF (Fig. 9e, f). Both the CRF and NRFC

due to all anthropogenic emissions are largely explained by the CRF and NRFC caused by change in emission of sulfur (compare Figs. 9c, d and 8c, d). The global average CRF is  $-0.28 \pm 0.04 \text{ W m}^{-2}$  due to the changes in all anthropogenic emissions, while the NRFC is slightly positive ( $0.08 \pm 0.02 \text{ W m}^{-2}$ ).

### 3.3 The influence of SOA on anthropogenic forcing

SOA particles have a strong potential to act as INPs and therefore influence the formation of cirrus clouds. We examined the radiative forcing of all anthropogenic aerosols on cirrus clouds when including the INPs from newly nucleated SOA particles. Figure 10 shows the column number concentration of INPs and zonal average of INPs from SOA in the PD and PI atmosphere. Changes in natural SOA precursors between the PI and PD atmospheres (i.e., isoprene,  $\alpha$ -pinene, and limonene emissions) are caused by changes in temperature as well as by changes in land use, while changes in aromatic emissions are associated with anthropogenic emission growth. In addition, newly formed SOA particles grow to accumulation mode size as a result of coagulation of particles (sulfate and other newly formed SOA particles), deposition of gaseous sulfate, and incorporation of other SOA compounds (e.g., through partitioning or kinetic uptake). Thus, the number concentration of INPs from SOA is much higher in the PD than that in the PI due to the much higher concentration of SOA in the accumulation mode in the PD (Zhu et al., 2019). The INPs from SOA are highest in the middle latitudes of the NH in the PD, while the INPs from SOA are higher in the SH than those in the NH in the PI atmosphere (Fig. 10a, b). The INPs from SOA in the PD are spread between 600 and 150 hPa with a peak around 300 hPa, so there is a possible influence on the formation of cirrus clouds (Fig. 10b). The INPs from SOA in the PI have a peak concentration that is a little higher than those in the PD (Fig. 10d). The global average  $N_i$  from heterogeneous nucleation increases by  $1.86 \times 10^8 \text{ m}^{-2}$  from PI to PD when including the INPs from SOA (Fig. 11e), which is in contrast to the decrease in the global average  $N_i$  from heterogeneous nucleation in the case without SOA (Fig. 5e). The INPs from SOA increase the  $N_i$  from heterogeneous nu-

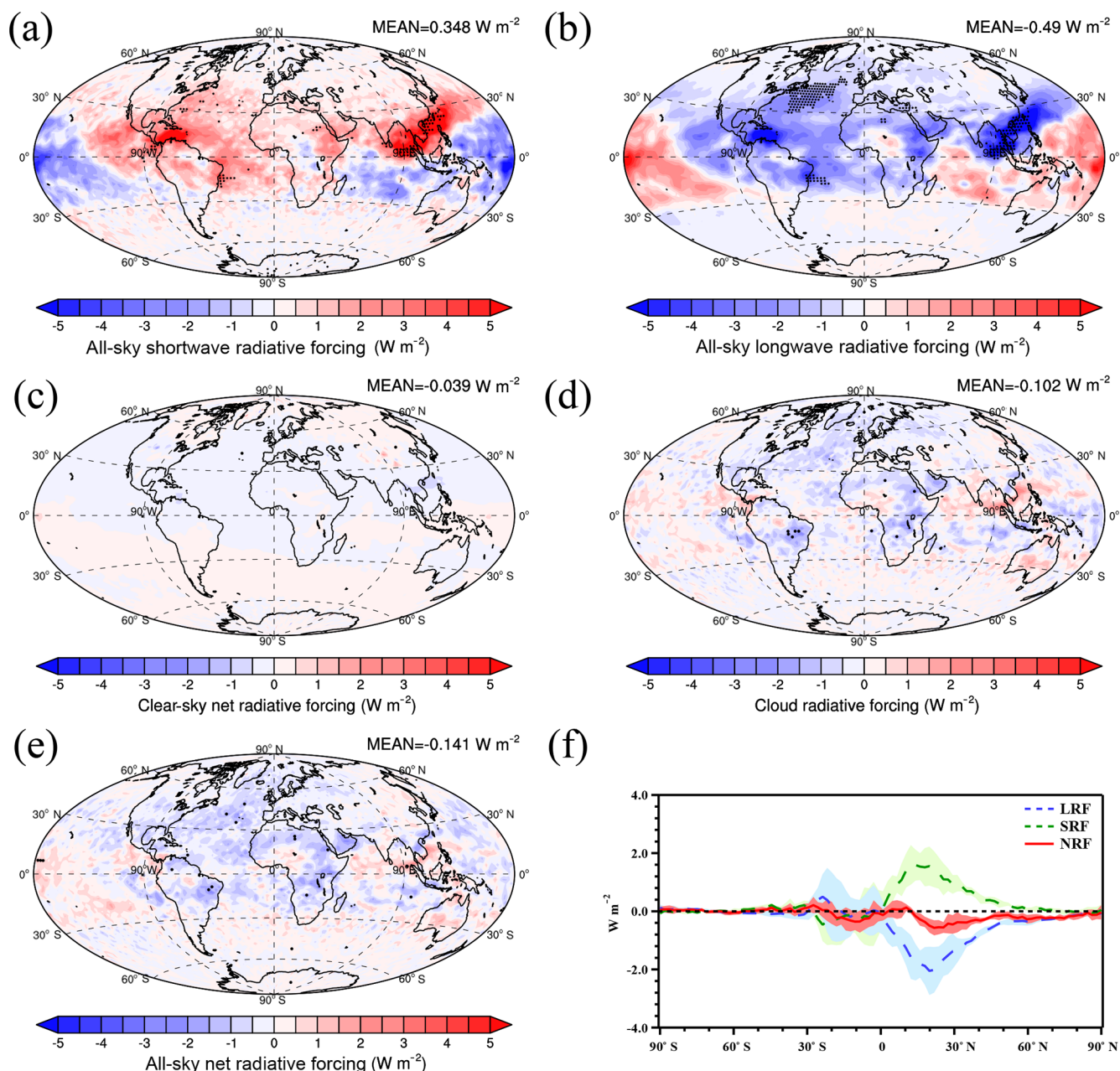


**Figure 7.** Annual mean plots of all-sky shortwave radiative forcing (a), all-sky longwave radiative forcing (b), clear-sky net radiative forcing (c), cloud radiative forcing (d), and all-sky net radiative forcing (e) as well as all-sky longwave radiative forcing (f, LRF, blue dashed line), all-sky shortwave radiative forcing (f, SRF, green dashed line), and all-sky net radiative forcing (f, NRF, red solid line) versus latitude for the difference between the PD\_Base and PI\_cSoot cases. Differences significant at the 90 % level according to a Student's *t* test are depicted by points. The shading in (f) represents 1 standard deviation of the interannual variation over 6 years.

creation in both the PD and PI cases when compared to the PD\_Base and PI\_ALL cases (Figs. S6e, S7e). However, the increase in  $N_i$  from heterogeneous nucleation in the PD is much larger than that in the PI because of the larger number concentration of INPs from SOA in the PD. As a result, the large increase in INPs from SOA between the PD and the PI enhances heterogeneous nucleation, resulting in

an increase in  $N_i$  from heterogeneous nucleation, especially in the tropics around 150 hPa and in the Antarctic from 400 to 200 hPa (Fig. 11f). The increase in the heterogeneous nucleation when including SOA widely inhibits homogeneous nucleation in both the PD and PI (Figs. S6c, S7c). In the PD, the increase in  $N_i$  from heterogeneous nucleation even outweighs the decrease in  $N_i$  from homogeneous nucleation,



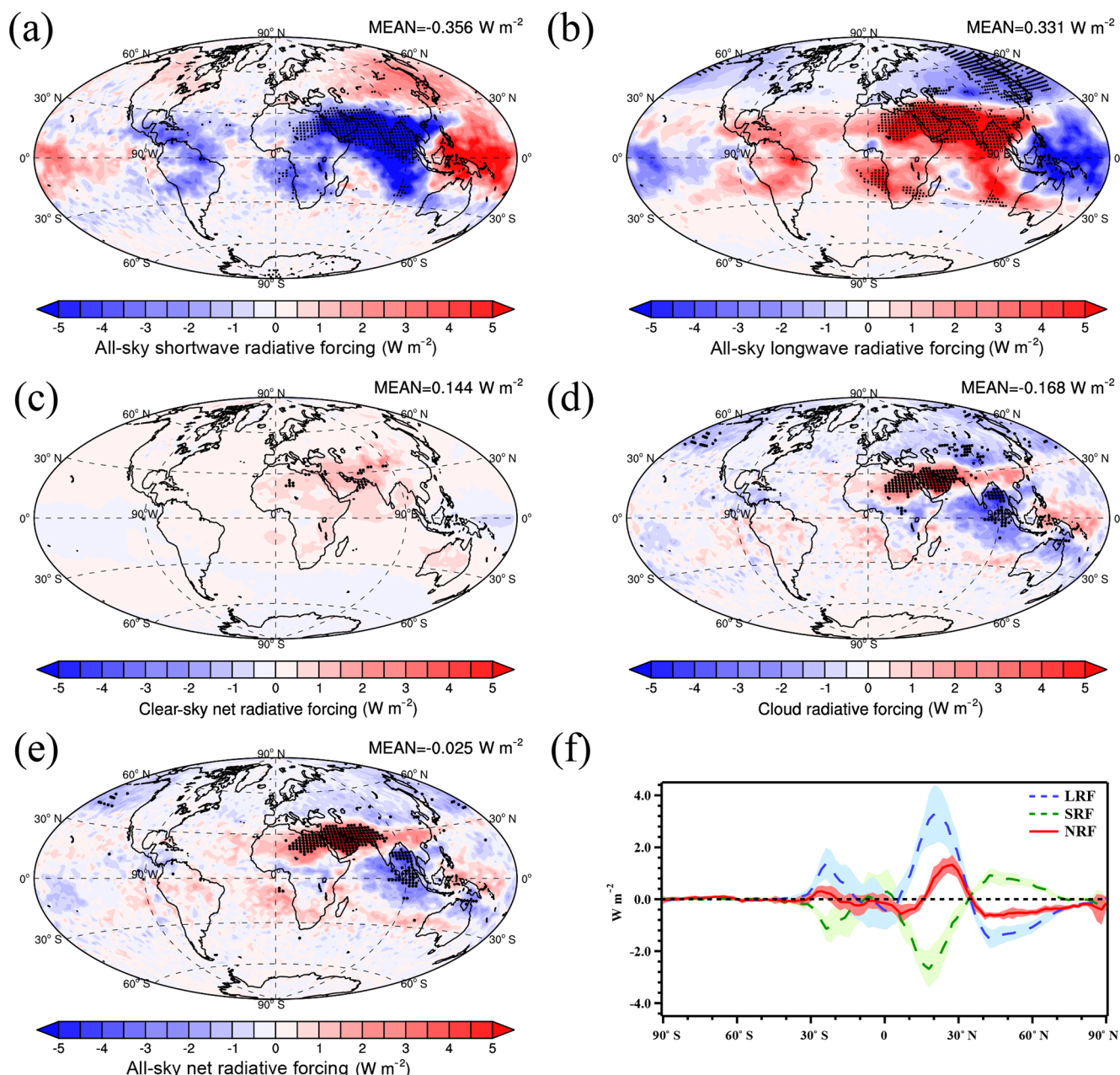


**Figure 8.** As in Fig. 7 but for the difference between the PD\_Base and PI\_SO4 cases. Differences significant at the 90 % level according to a Student's  $t$  test are depicted by points. The shading in (f) represents 1 standard deviation of the interannual variation over 6 years.

leading to an increase of  $0.4 \times 10^8 \text{ m}^{-2}$  in the global average  $N_i$  due to SOA compared to the PD\_Base case (Fig. S6a). In contrast, the INPs from SOA in the PI case make a larger contribution to the decrease in  $N_i$  from homogeneous nucleation than the increase in  $N_i$  from heterogeneous nucleation, resulting in a decrease in total  $N_i$  of  $-0.31 \times 10^8 \text{ m}^{-2}$  compared to the PI\_ALL case (Fig. S7a). The inclusion of INPs from SOA decreases  $N_i$  in the tropics but increases  $N_i$  in the middle to high latitudes in both the NH and SH (Figs. S6b, S7b). The global average  $N_i$  in the PD increases while the

global average  $N_i$  in the PI is decreased. Both changes are caused by additional INPs from SOA (Figs. S6a, S7a) resulting in a larger increase in the global average  $N_i$  from the PI to PD compared to the case without SOA (compare Figs. 5a and 11a). When including INPs from SOA,  $N_i$  increases to a large extent over South Asia, and the north Indian Ocean  $N_i$  decreases over the middle to high latitudes of East Asia and the North Pacific Ocean (compare Figs. 11a and 5a).

The increased  $N_i$  leads to a significant increase in the IWP in South Asia, the north Indian Ocean, and Antarctica due

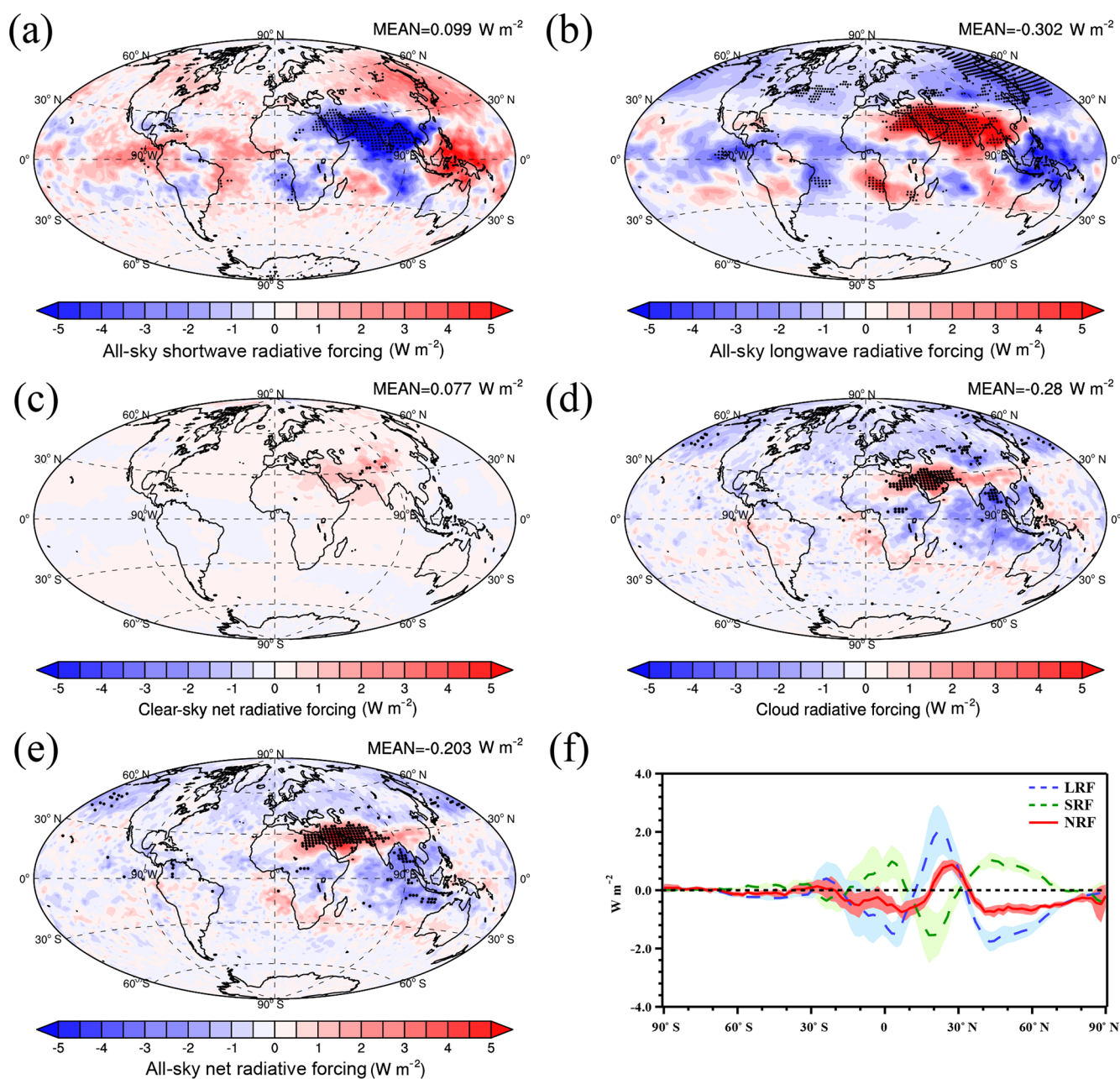


**Figure 9.** As in Fig. 7 but for the difference between the PD\_Base and PI\_ALL cases. Differences significant at the 90 % level according to a Student's *t* test are depicted by points. The shading in (f) represents 1 standard deviation of the interannual variation over 6 years.

to the reduction of gravitational removal, while the IWP decreases significantly in the middle to high latitudes of East Asia, which is caused by the decrease in  $N_i$  (Fig. 11a). Compared with the case without SOA (PD\_Base-PI\_ALL), the inclusion of SOA increases the difference in the IWP between the PD and PI in Antarctica significantly because of the increase in  $N_i$  from heterogeneous nucleation of INPs from SOA there (Fig. 12a). The change in the LWP due to dynamic feedbacks in the case with SOA is significant in only a few grids, which is similar to the case without SOA (Fig. 12c).

The larger increases in  $N_i$  and IWP over South Asia and the north Indian Ocean lead to the larger changes in both SRF and LRF when including SOA compared to the case without SOA, while the significant decrease in  $N_i$  in the middle to high latitudes over East Asia leads to a significant decrease in the LRF. The increase in  $N_i$  and IWP in Antarctica only increases the LRF but does not change the SRF because of the very low shortwave flux in polar regions (Fig. 12c, d). The larger decrease in the SRF offsets the increase in the LRF in the tropics when including SOA, resulting in a simi-



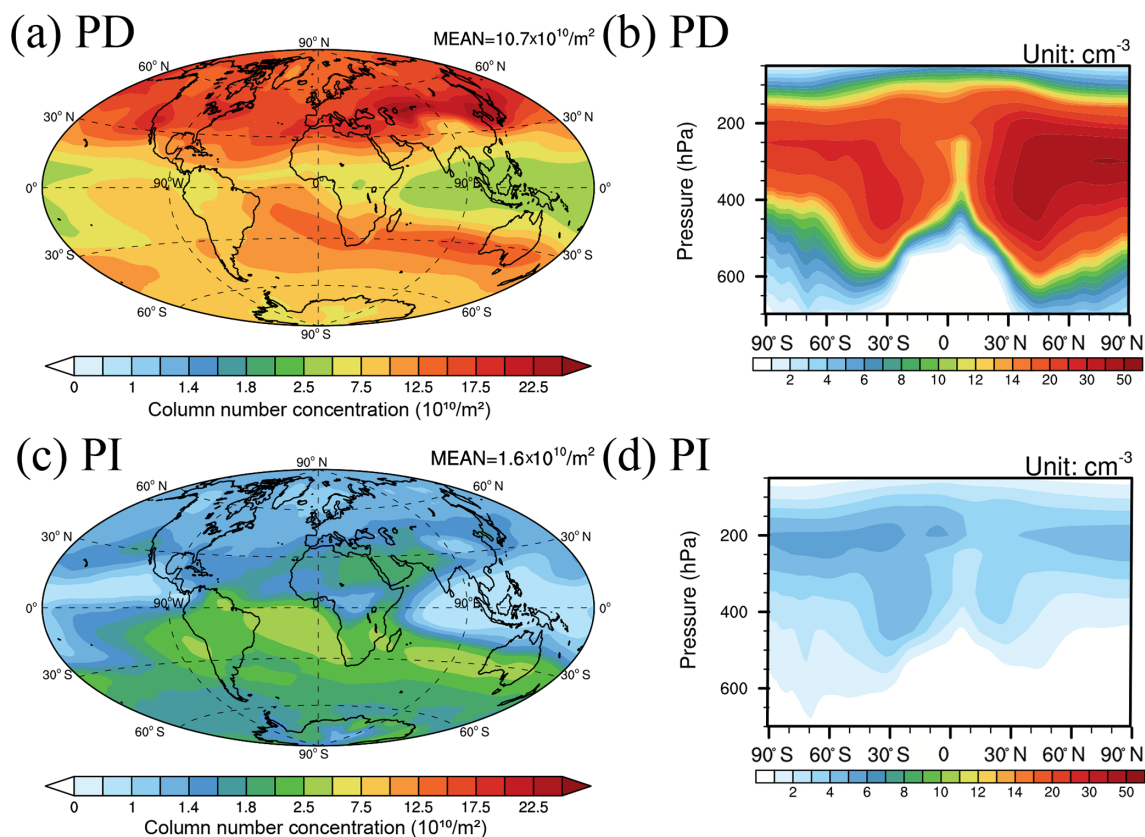


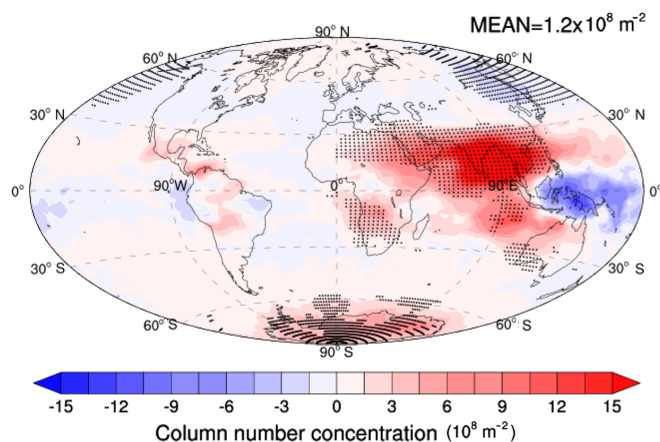
**Figure 10.** The vertically integrated number of INPs (a, c) and zonal average plots of INPs (b, d) from SOA in the PD\_SOA (a, b) and PI\_SOA (c, d) cases.

lar value for NRF in the tropics for the cases with and without SOA (Fig. 13f). However, the more positive changes in the LRF from PI to PD in Antarctica and the Arctic when including SOA explain the more positive NRF there compared to the case without SOA (Fig. 13f). In addition, the NRF in South Asia and North Africa around  $30^\circ$  N, where NRF is most positive in the case without SOA, becomes even more positive when including SOA due to the larger increases in  $N_i$ . As a result, the significant and larger positive NRF over Antarctica as well as South Asia and North Africa around  $30^\circ$  N causes an increase in the global average NRF due to all anthropogenic aerosol to  $-0.04 \pm 0.08 \text{ W m}^{-2}$  when including SOA compared to the value of  $-0.20 \pm 0.05 \text{ W m}^{-2}$  in the case without SOA. The NRF when including SOA is up to  $6.6 \text{ W m}^{-2}$  in the Arabian Peninsula while it is as low as  $-4.8 \text{ W m}^{-2}$  in the north Indian Ocean (Fig. 12g). Compared to the case without SOA, the global average CRF is less negative ( $-0.14 \pm 0.07 \text{ W m}^{-2}$  compared to  $-0.28 \text{ W m}^{-2}$ ) largely due to the significant positive CRF over Antarctica (Fig. 12f). Simultaneously, the NRFC is more positive in the case with SOA than the case without SOA, which offset 73 % of the CRF (Fig. 12e).

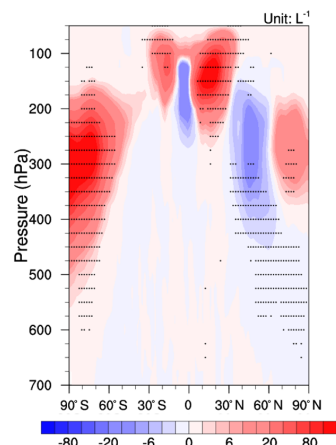
#### 4 Conclusion and discussion

This work develops a new ice nucleation parameterization, HYBRID, which is a combination of the LP and KL parameterizations. The global model using this new scheme is able to simulate the growth and decay of ice particles in the updrafts and downdrafts associated with gravity waves as in the modified KL scheme (Penner et al., 2018) and is able to treat the changes in aerosol number concentration from freezing haze particles with fidelity in the sign of the change as in the LP scheme. The HYBRID scheme overcomes some of the deficiencies in previous ice nucleation schemes. We evaluated the HYBRID ice nucleation scheme by comparing the scheme with the Liu and Penner (2005) adiabatic parcel model and by comparing its global predictions using observed  $N_i$ . We used 10 000 parcel model simulations to show that the HYBRID box model predicts 7.3 % larger  $N_i$  than the LP adiabatic parcel model with 21.5 % larger  $N_i$  from homogeneous nucleation. The global model using the HYBRID scheme overestimates  $N_i$  between 195 and 215 K somewhat compared to observations, as do earlier simulations with only the KL scheme (Penner et al., 2018). The results of  $N_i$  from the HYBRID scheme are in reasonable agreement with observations and thus were used in the CESM/IMPACT global

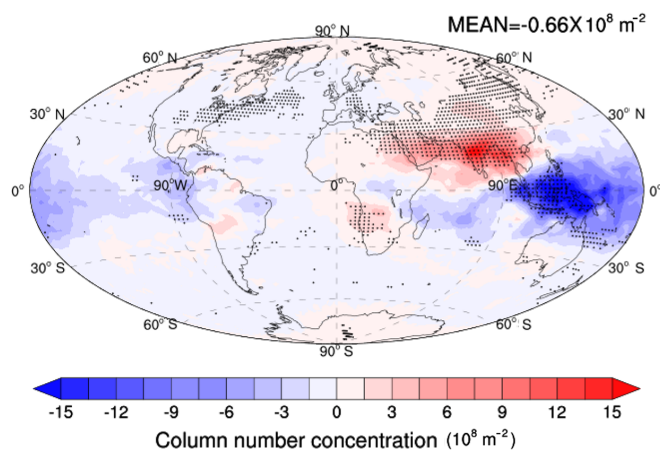
(a) Total Ni



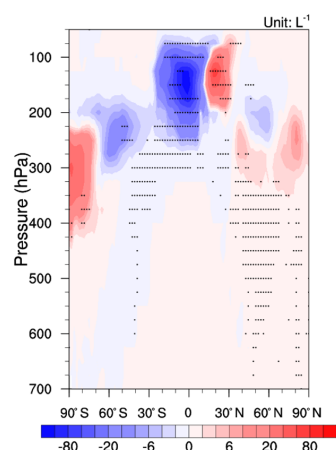
(b) Total Ni



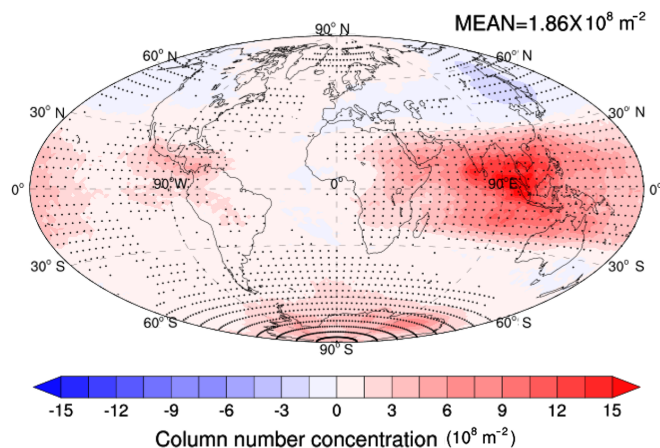
(c) Homogeneous nucleation



(d) Homogeneous nucleation



(e) Heterogeneous nucleation



(f) Heterogeneous nucleation

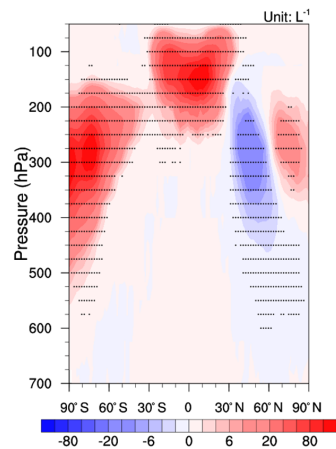


**Figure 11.** The annual average change in column number concentration (**a, c, e**) and zonal average number concentration (**b, d, f**) of total ice (**a, b**), ice from homogeneous nucleation (**c, d**), and ice from heterogeneous nucleation (**e, f**) for the difference between the PD\_SOA and PI\_SOA cases. Differences significant at the 90 % level according to a Student's *t* test are depicted by points.

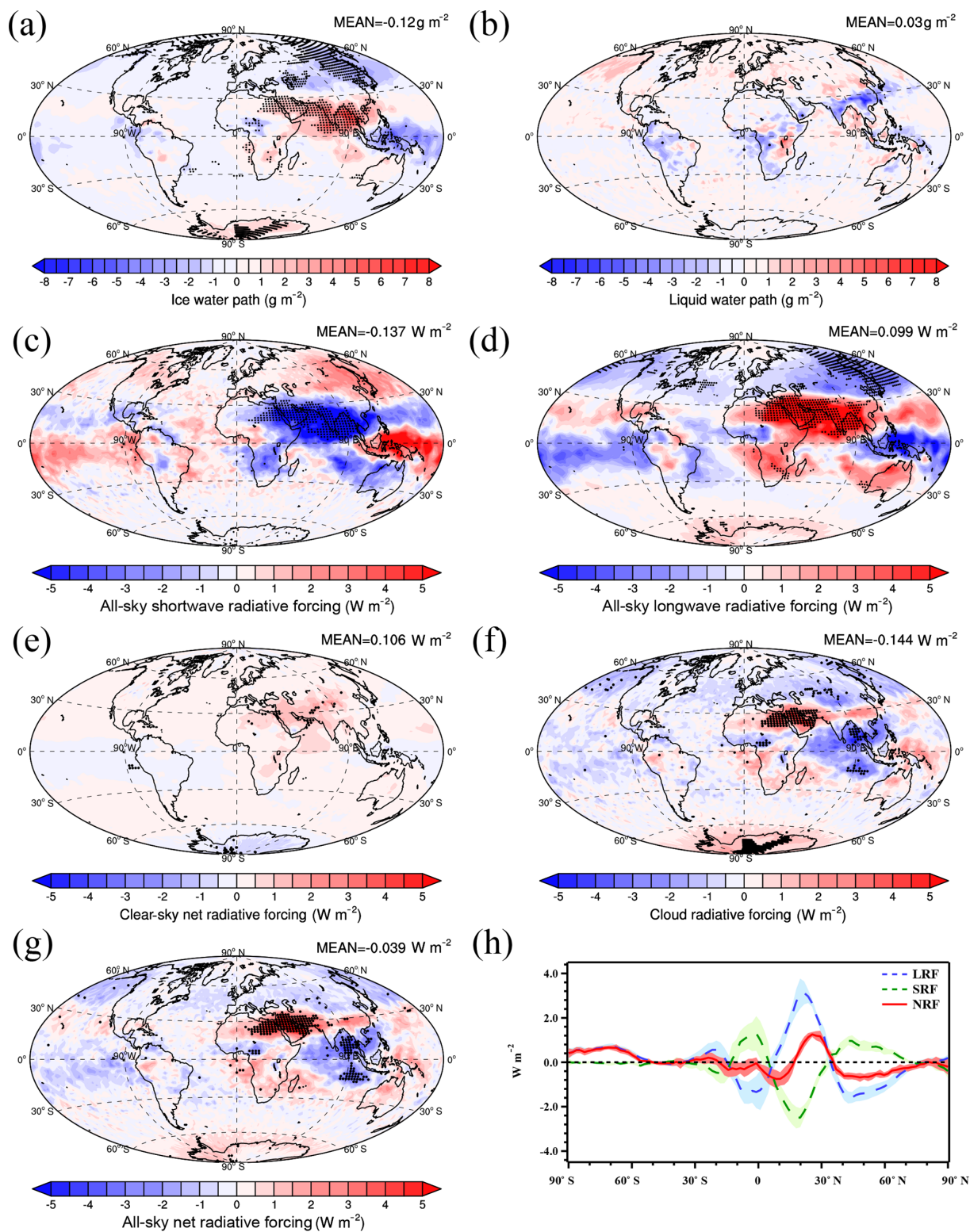


**Figure 12.** Annual mean plots of the changes in ice water path (a), liquid water path (b), all-sky shortwave radiative forcing (c), all-sky longwave radiative forcing (d), clear-sky net radiative forcing (e), cloud radiative forcing (f), and all-sky net radiative forcing (g) as well as longwave radiative forcing (h, LRF, blue dashed line), shortwave radiative forcing (h, SRF, green dashed line), and all-sky net radiative forcing (h, NRF, red solid line) versus latitude for the difference between the PD\_SOA and PI\_SOA cases. Differences significant at the 90 % level according to a Student's *t* test are depicted by points. The shading in (h) represents 1 standard deviation of the interannual variation over 6 years.



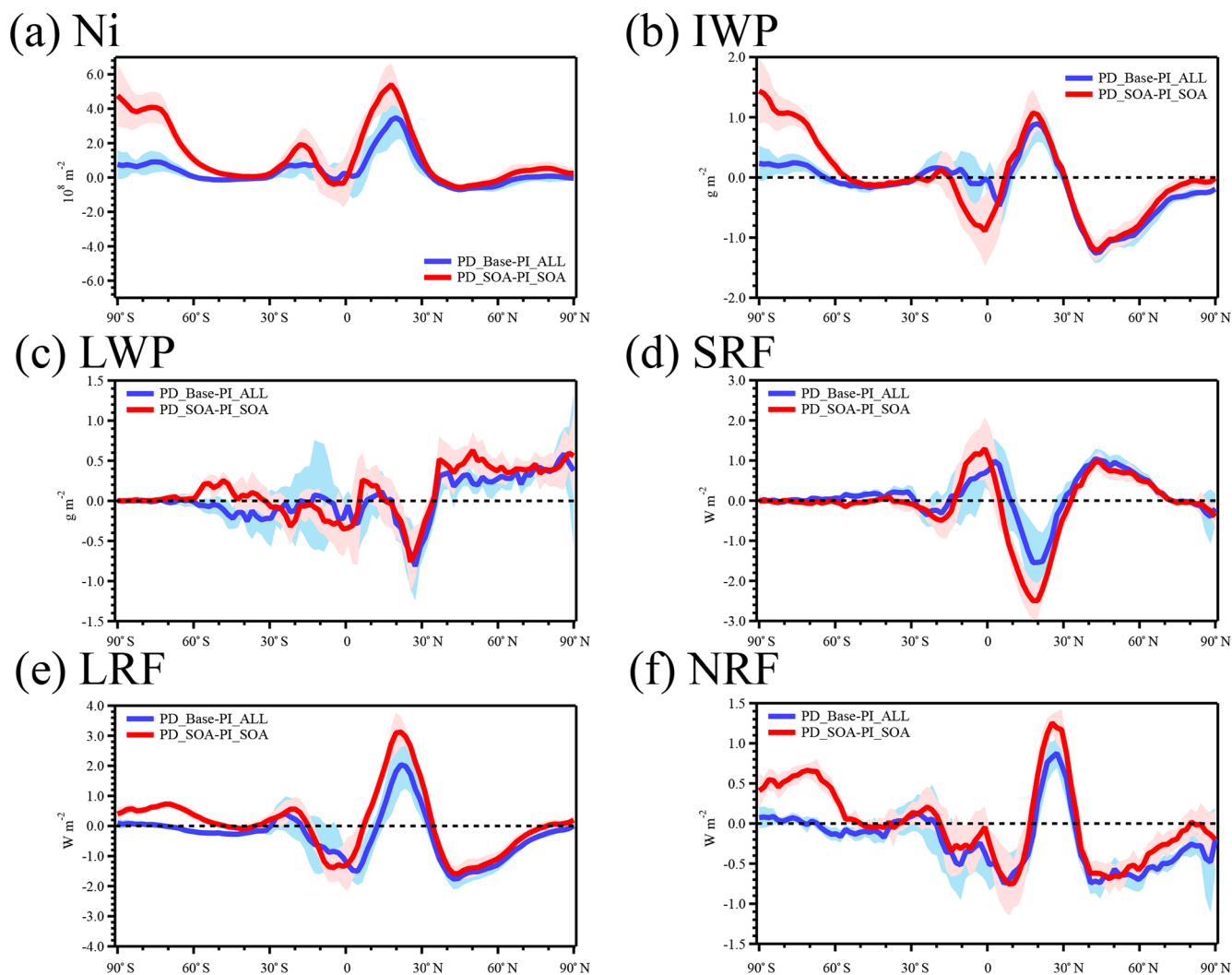


**Figure 13.** Change in vertically integrated ice number concentration (a), ice water path (b), liquid water path (c), and shortwave radiative forcing (d), longwave radiative forcing (e), and all-sky net radiative forcing (f) for the difference between the PD\_SOA and PI\_SOA cases (red line) as well as the PD\_Base and PI\_ALL cases (blue line). The shading represents 1 standard deviation of the interannual variation over 6 years.

model to estimate the radiative forcing of aerosols in large-scale cirrus clouds. The predicted  $N_i$  depends on the competition between homogeneous and heterogeneous nucleation. These two ice nucleation processes dominate the formation of  $N_i$  in different regions and altitudes. The global average  $N_i$  is dominated by homogeneous nucleation in the PD atmosphere.

We performed a series of model experiments using the HYBRID ice nucleation scheme to explore the forcing and cloud changes associated with changes in aircraft soot, sulfur emissions and all anthropogenic emissions from the PI to PD. Results are summarized in Table 3. The INPs from aircraft soot usually decrease  $N_i$  by the inhibition of homogeneous nucleation in spite of some areas with small increases in  $N_i$ . In contrast, the increase in sulfur emissions from PI to PD en-

hances homogeneous nucleation in most regions and leads to a small decrease in the  $N_i$  formed as a result of heterogeneous nucleation. We found that the effect of aerosols in cirrus clouds could feed back to the meteorological state as determined by temperature and  $\text{RH}_i$ , which could have an opposite effect on the changes in  $N_i$  due to either aircraft soot or sulfur emissions in the remote regions like the west Pacific Ocean. These meteorological feedbacks partly reduce the changes in the global average  $N_i$  due to anthropogenic emissions. The changes in  $N_i$  from PI to PD caused by all anthropogenic emissions are dominated by the changes due to the sulfur emissions, but the changes in surface and aircraft soot emission have some effects on the inhibition of homogeneous nucleation.

The changes in  $N_i$  due to anthropogenic aerosols lead to changes in IWP as well as LWP due to dynamical feedbacks. The changes in SRF and LRF are always determined by the changes in the IWP (and  $N_i$ ), but the changes in LWP could either enhance or offset the effects of IWP on the radiative fluxes. Emissions of aircraft soot lead to a positive change in the global average SRF while the global average LRF is negative. The changes in sulfur emissions from the PI to PD atmosphere lead to opposite changes in the global average SRF and LRF compared to aircraft soot because of the different signs of changes in  $N_i$ . The total net forcing in cirrus clouds is usually dominated by LRF but it is dominated by SRF when the changes in warm clouds cause a feedback that reinforces the effect of cirrus clouds on shortwave fluxes. As a result, the emission of aircraft soot has a negative global average NRF of  $-0.14 \pm 0.07 \text{ W m}^{-2}$  in large-scale cirrus clouds, while the changes in the sulfur emissions from the PI to the PD lead to a small negative global average NRF of  $-0.02 \pm 0.06 \text{ W m}^{-2}$ . The global average NRF due to all anthropogenic emissions from PI to PD, which is estimated to be  $-0.20 \pm 0.05 \text{ W m}^{-2}$ , is dominated by the NRF caused by increased sulfur emissions but is more negative than the forcing by sulfur emissions alone due to changes in the emissions of soot.

The influence of SOA on the anthropogenic forcing of aerosols in large-scale cirrus clouds was examined. The additional INPs from SOA increase the  $N_i$  from heterogeneous nucleation and decrease  $N_i$  from homogeneous nucleation, but the sign of the changes in the total  $N_i$  depends on the balance of these two effects. The high number concentration of INPs from SOA in the PD atmosphere causes an increase in  $N_i$  compared to not including INPs from SOA while the low number concentration in the PI atmosphere causes a decrease. As a result, the changes in  $N_i$  due to the changes in anthropogenic emissions from PI to PD are larger when including INPs from SOA than the case without SOA. The inclusion of SOA mainly increases the changes in the NRF in the polar regions and the regions around  $30^\circ \text{ N}$ , resulting in a less negative NRF of  $-0.04 \pm 0.07 \text{ W m}^{-2}$  associated with the change in all anthropogenic emissions.

The radiative forcing of anthropogenic aerosols' effect on cirrus clouds estimated in this study is less negative than the result indicated in Penner et al. (2009) ( $-0.38$  to  $-0.56 \text{ W m}^{-2}$ ) and has a different sign compared with the result shown in Gettelman et al. (2012) ( $0.27 \pm 0.10 \text{ W m}^{-2}$ ). This is mostly caused by the different treatments for updraft velocity, the concentration of haze particles, and INPs as well as the application of a different ice nucleation scheme. Current models show that homogeneous nucleation dominates the formation of new ice particles in most regions over the world with the largest contribution to cirrus cloud formation in the tropical upper troposphere (Zhou et al., 2016; Shi and Liu, 2018; Shi et al., 2015). However, some observations indicated the importance and high occurrence frequency of heterogeneous nucleation in the tropical tropopause region

(Jensen et al., 2013). Although the inclusion of INPs from newly formed SOA in this study inhibits homogeneous nucleation in the tropics, homogeneous nucleation is still responsible for 75 % of total  $N_i$  in the PD atmosphere. Laboratory measurements have supported other species acting as INPs and enhancing heterogeneous nucleation such as solid ammonium sulfate (Abbatt et al., 2006), which has not been considered in current global climate models. Additional INPs from anthropogenic ammonium sulfate can be expected to increase the anthropogenic forcing in cirrus clouds to be less negative and possibly even positive. The HYBRID ice nucleation scheme somewhat overestimates the ice number concentration produced from homogeneous nucleation compared to a full parcel model. An explicit representation of the ice nucleation process used in the global climate model may be helpful to predict the ice number and therefore radiation budget more correctly in the future. The ability of SOA to act as an INP probably varies depending on the property of different SOA compounds as well as their particle size and mixing state (Baustian et al., 2013; Berkemeier et al., 2014; Charnawskas et al., 2017; Shiraiwa et al., 2017). A global climate model coupled online with the formation mechanism of SOA together with an increased understanding of the ability of SOA to act as an INP would help in estimating the contribution of SOA to ice particle formation more accurately.

*Code and data availability.* The CESM1.2.2 model and related documentation can be download from <http://www.cesm.ucar.edu/models/cesm1.2/> (last access: November 2019; CESM, 2017). Model input data can be download from <https://svn-ccsm-inputdata.cgd.ucar.edu/trunk/inputdata/> (last access: November 2019; CESM, 2017). Observational datasets, source code, and simulation results are available upon request from the corresponding author (zhujialei@tju.edu.cn).

*Supplement.* The supplement related to this article is available online at: <https://doi.org/10.5194/acp-20-7801-2020-supplement>.

*Author contributions.* JZ developed the model, performed the simulations, and analyzed all data. JEP guided the model development and data analysis. Both authors contributed to writing the paper.

*Competing interests.* The authors declare that they have no conflict of interest.

*Acknowledgements.* Computer time was provided by the NCAR CISL.

*Financial support.* This research has been supported by the National Aeronautics and Space Administration (grant no.

NNX15AE34G), the National Science Foundation, Directorate for Geosciences (grant no. 1540954), and the Startup Foundation of Tianjin University (grant no. 390/0903061032).

*Review statement.* This paper was edited by Martina Krämer and reviewed by two anonymous referees.

## References

- Abbatt, J., Benz, S., Cziczo, D., Kanji, Z., Lohmann, U., and Möhler, O.: Solid ammonium sulfate aerosols as ice nuclei: A pathway for cirrus cloud formation, *Science*, 313, 1770–1773, 2006.
- Andreae, M. O., Afchine, A., Albrecht, R., Holanda, B. A., Artaxo, P., Barbosa, H. M. J., Borrmann, S., Cecchini, M. A., Costa, A., Dollner, M., Fütterer, D., Järvinen, E., Jurkat, T., Klimach, T., Konemann, T., Knote, C., Krämer, M., Krisna, T., Machado, L. A. T., Mertes, S., Minikin, A., Pöhlker, C., Pöhlker, M. L., Pöschl, U., Rosenfeld, D., Sauer, D., Schlager, H., Schnaiter, M., Schneider, J., Schulz, C., Spanu, A., Sperling, V. B., Voigt, C., Walser, A., Wang, J., Weinzierl, B., Wendisch, M., and Ziereis, H.: Aerosol characteristics and particle production in the upper troposphere over the Amazon Basin, *Atmos. Chem. Phys.*, 18, 921–961, <https://doi.org/10.5194/acp-18-921-2018>, 2018.
- Barahona, D. and Nenes, A.: Parameterization of cirrus cloud formation in large-scale models: Homogeneous nucleation, *J. Geophys. Res.-Atmos.*, 113, D11211, <https://doi.org/10.1029/2007JD009355>, 2008.
- Barrett, S., Prather, M., Penner, J., Selkirk, H., Balasubramanian, S., Dopelheuer, A., Fleming, G., Gupta, M., Halthore, R., and Hileman, J.: Guidance on the use of AEDT gridded aircraft emissions in atmospheric models, A technical note submitted to the US Federal Aviation Administration, Massachusetts Institute of Technology (MIT), 2010.
- Baustian, K. J., Wise, M. E., Jensen, E. J., Schill, G. P., Freedman, M. A., and Tolbert, M. A.: State transformations and ice nucleation in amorphous (semi-)solid organic aerosol, *Atmos. Chem. Phys.*, 13, 5615–5628, <https://doi.org/10.5194/acp-13-5615-2013>, 2013.
- Berkemeier, T., Shiraiwa, M., Pöschl, U., and Koop, T.: Competition between water uptake and ice nucleation by glassy organic aerosol particles, *Atmos. Chem. Phys.*, 14, 12513–12531, <https://doi.org/10.5194/acp-14-12513-2014>, 2014.
- Boville, B. A., Rasch, P. J., Hack, J. J., and McCaa, J. R.: Representation of clouds and precipitation processes in the Community Atmosphere Model version 3 (CAM3), *J. Climate*, 19, 2184–2198, 2006.
- Cantrell, W. and Heymsfield, A.: Production of ice in tropospheric clouds: A review, *B. Am. Meteorol. Soc.*, 86, 795–808, 2005.
- CESM: CESM1.2 Series Public Release, UCAR/NCAR, available at: <http://www.cesm.ucar.edu/models/cesm1.2/> (last access: November 2019), 2017.
- Charnawskas, J. C., Alpert, P. A., Lambe, A. T., Berkemeier, T., O'Brien, R. E., Massoli, P., Onasch, T. B., Shiraiwa, M., Moffet, R. C., Gilles, M. K., Davidovits, P., Worsnop, D. R., and Knopf, D. A.: Condensed-phase biogenic-anthropogenic interactions with implications for cold cloud formation, *Faraday Discuss.*, 200, 165–194, <https://doi.org/10.1039/c7fd00010c>, 2017.
- Cziczo, D. J., Murphy, D. M., Hudson, P. K., and Thomson, D. S.: Single particle measurements of the chemical composition of cirrus ice residue during CRYSTAL-FACE, *J. Geophys. Res.-Atmos.*, 109, D04201, <https://doi.org/10.1029/2003jd004032>, 2004.
- Cziczo, D. J., Froyd, K. D., Hoose, C., Jensen, E. J., Diao, M., Zondlo, M. A., Smith, J. B., Twohy, C. H., and Murphy, D. M.: Clarifying the dominant sources and mechanisms of cirrus cloud formation, *Science*, 340, 1320–1324, 2013.
- DeMott, P., Cziczo, D., Prenni, A., Murphy, D., Kreidenweis, S., Thomson, D., Borys, R., and Rogers, D.: Measurements of the concentration and composition of nuclei for cirrus formation, *P. Natl. Acad. Sci. USA*, 100, 14655–14660, 2003.
- Fan, J., Wang, Y., Rosenfeld, D., and Liu, X.: Review of aerosol–cloud interactions: Mechanisms, significance, and challenges, *J. Atmos. Sci.*, 73, 4221–4252, 2016.
- Gary, B. L.: Mesoscale temperature fluctuations in the stratosphere, *Atmos. Chem. Phys.*, 6, 4577–4589, <https://doi.org/10.5194/acp-6-4577-2006>, 2006.
- Gary, B. L.: Mesoscale temperature fluctuations in the Southern Hemisphere stratosphere, *Atmos. Chem. Phys.*, 8, 4677–4681, <https://doi.org/10.5194/acp-8-4677-2008>, 2008.
- Gettelman, A., Liu, X., Barahona, D., Lohmann, U., and Chen, C.: Climate impacts of ice nucleation, *J. Geophys. Res.-Atmos.*, 117, D20201, <https://doi.org/10.1029/2012jd017950>, 2012.
- Gordon, H., Sengupta, K., Rap, A., Duplissy, J., Frege, C., Williamson, C., Heinritzi, M., Simon, M., Yan, C., Almeida, J., Trostl, J., Nieminen, T., Ortega, I. K., Wagner, R., Dunne, E. M., Adamov, A., Amorim, A., Bernhammer, A. K., Bianchi, F., Breitenlechner, M., Brilke, S., Chen, X., Craven, J. S., Dias, A., Ehrhart, S., Fischer, L., Flagan, R. C., Franchin, A., Fuchs, C., Guida, R., Hakala, J., Hoyle, C. R., Jokinen, T., Junninen, H., Kangasluoma, J., Kim, J., Kirkby, J., Krapf, M., Kurten, A., Laaksonen, A., Lehtipalo, K., Makhmutov, V., Mathot, S., Molteni, U., Monks, S. A., Onnela, A., Perakyla, O., Piel, F., Petaja, T., Praplan, A. P., Pringle, K. J., Richards, N. A., Rissanen, M. P., Rondo, L., Sarnela, N., Schobesberger, S., Scott, C. E., Seinfeld, J. H., Sharma, S., Sipila, M., Steiner, G., Stozhkov, Y., Stratmann, F., Tome, A., Virtanen, A., Vogel, A. L., Wagner, A. C., Wagner, P. E., Weingartner, E., Wimmer, D., Winkler, P. M., Ye, P., Zhang, X., Hansel, A., Dommen, J., Donahue, N. M., Worsnop, D. R., Baltensperger, U., Kulmala, M., Curtius, J., and Carslaw, K. S.: Reduced anthropogenic aerosol radiative forcing caused by biogenic new particle formation, *P. Natl. Acad. Sci. USA*, 113, 12053–12058, <https://doi.org/10.1073/pnas.1602360113>, 2016.
- Hendricks, J., Kärcher, B., and Lohmann, U.: Effects of ice nuclei on cirrus clouds in a global climate model, *J. Geophys. Res.*, 116, D18206, <https://doi.org/10.1029/2010jd015302>, 2011.
- Hoesly, R. M., Smith, S. J., Feng, L., Klimont, Z., Janssens-Maenhout, G., Pitkanen, T., Seibert, J. J., Vu, L., Andres, R. J., Bolt, R. M., Bond, T. C., Dawidowski, L., Kholod, N., Kurokawa, J.-I., Li, M., Liu, L., Lu, Z., Moura, M. C. P., O'Rourke, P. R., and Zhang, Q.: Historical (1750–2014) anthropogenic emissions of reactive gases and aerosols from the Community Emissions Data System (CEDS), *Geosci. Model Dev.*, 11, 369–408, <https://doi.org/10.5194/gmd-11-369-2018>, 2018.

- Hong, Y., Liu, G., and Li, J. L.: Assessing the radiative effects of global ice clouds based on CloudSat and CALIPSO measurements, *J. Climate*, 29, 7651–7674, 2016.
- Hoose, C. and Möhler, O.: Heterogeneous ice nucleation on atmospheric aerosols: a review of results from laboratory experiments, *Atmos. Chem. Phys.*, 12, 9817–9854, <https://doi.org/10.5194/acp-12-9817-2012>, 2012.
- Ignatius, K., Kristensen, T. B., Järvinen, E., Nichman, L., Fuchs, C., Gordon, H., Herenz, P., Hoyle, C. R., Duplissy, J., Garimella, S., Dias, A., Frege, C., Höppl, N., Tröstl, J., Wagner, R., Yan, C., Amorim, A., Baltensperger, U., Curtius, J., Donahue, N. M., Gallagher, M. W., Kirkby, J., Kulmala, M., Möhler, O., Saathoff, H., Schnaiter, M., Tomé, A., Virtanen, A., Worsnop, D., and Stratmann, F.: Heterogeneous ice nucleation of viscous secondary organic aerosol produced from ozonolysis of  $\alpha$ -pinene, *Atmos. Chem. Phys.*, 16, 6495–6509, <https://doi.org/10.5194/acp-16-6495-2016>, 2016.
- IPCC: Climate Change 2013: The Physical Science Basis. Contribution of Working Group I to the Fifth Assessment Report of the Intergovernmental Panel on Climate Change, Cambridge University Press, Cambridge, United Kingdom and New York, NY, USA, 1535 pp., 2013.
- Jensen, E. J., Diskin, G., Lawson, R. P., Lance, S., Bui, T. P., Hlavka, D., McGill, M., Pfister, L., Toon, O. B., and Gao, R.: Ice nucleation and dehydration in the Tropical Tropopause Layer, *P. Natl. Acad. Sci. USA*, 110, 2041–2046, <https://doi.org/10.1073/pnas.1217104110>, 2013.
- Joos, H., Spichtinger, P., Lohmann, U., Gayet, J. F., and Minikin, A.: Orographic cirrus in the global climate model ECHAM5, *J. Geophys. Res.-Atmos.*, 113, D18205, <https://doi.org/10.1029/2007JD009605>, 2008.
- Kärcher, B. and Lohmann, U.: A parameterization of cirrus cloud formation: Homogeneous freezing of supercooled aerosols, *J. Geophys. Res.-Atmos.*, 107, AAC 4-1–AAC 4-10, 2002.
- Kärcher, B., Hendricks, J., and Lohmann, U.: Physically based parameterization of cirrus cloud formation for use in global atmospheric models, *J. Geophys. Res.*, 111, D01205, <https://doi.org/10.1029/2005jd006219>, 2006.
- Knopf, D. A., Alpert, P. A., and Wang, B.: The Role of Organic Aerosol in Atmospheric Ice Nucleation: A Review, *ACS Earth and Space Chemistry*, 2, 168–202, <https://doi.org/10.1021/acsearthspacechem.7b00120>, 2018.
- Koehler, K. A., DeMott, P. J., Kreidenweis, S. M., Popovicheva, O. B., Petters, M. D., Carrico, C. M., Kireeva, E. D., Khokhlova, T. D., and Shonija, N. K.: Cloud condensation nuclei and ice nucleation activity of hydrophobic and hydrophilic soot particles, *Phys. Chem. Chem. Phys.*, 11, 7906–7920, 2009.
- Koop, T., Luo, B. P., Tsias, A., and Peter, T.: Water activity as the determinant for homogeneous ice nucleation in aqueous solutions, *Nature*, 406, 611–614, <https://doi.org/10.1038/35020537>, 2000.
- Koop, T., Bookhold, J., Shiraiwa, M., and Pöschl, U.: Glass transition and phase state of organic compounds: dependency on molecular properties and implications for secondary organic aerosols in the atmosphere, *Phys. Chem. Chem. Phys.*, 13, 19238–19255, <https://doi.org/10.1039/c1cp22617g>, 2011.
- Krämer, M., Schiller, C., Afchine, A., Bauer, R., Gensch, I., Mangold, A., Schlicht, S., Spelten, N., Sitnikov, N., Borrmann, S., de Reus, M., and Spichtinger, P.: Ice supersaturations and cirrus cloud crystal numbers, *Atmos. Chem. Phys.*, 9, 3505–3522, <https://doi.org/10.5194/acp-9-3505-2009>, 2009.
- Krämer, M., Rolf, C., Luebke, A., Afchine, A., Spelten, N., Costa, A., Meyer, J., Zöger, M., Smith, J., Herman, R. L., Buchholz, B., Ebert, V., Baumgardner, D., Borrmann, S., Klingebiel, M., and Avallone, L.: A microphysics guide to cirrus clouds – Part I: Cirrus types, *Atmos. Chem. Phys.*, 16, 3463–3483, <https://doi.org/10.5194/acp-16-3463-2016>, 2016.
- Krämer, M., Rolf, C., Spelten, N., Afchine, A., Fahey, D., Jensen, E., Khaykin, S., Kuhn, T., Lawson, P., Lykov, A., Pan, L. L., Riese, M., Rollins, A., Strohm, F., Thornberry, T., Wolf, V., Woods, S., Spichtinger, P., Quaas, J., and Sourdeval, O.: A Microphysics Guide to Cirrus – Part II: Climatologies of Clouds and Humidity from Observations, *Atmos. Chem. Phys. Discuss.*, <https://doi.org/10.5194/acp-2020-40>, in review, 2020.
- Kristjánsson, J. E., Edwards, J. M., and Mitchell, D. L.: Impact of a new scheme for optical properties of ice crystals on climates of two gems, *J. Geophys. Res.*, 105, 10063–10079, 2000.
- Kuebbeler, M., Lohmann, U., Hendricks, J., and Kärcher, B.: Dust ice nuclei effects on cirrus clouds, *Atmos. Chem. Phys.*, 14, 3027–3046, <https://doi.org/10.5194/acp-14-3027-2014>, 2014.
- Li, J. L. F., Waliser, D. E., Chen, W. T., Guan, B., Kubar, T., Stephens, G., Ma, H. Y., Deng, M., Donner, L., Seman, C., and Horowitz, L.: An observationally based evaluation of cloud ice water in CMIP3 and CMIP5 GCMs and contemporary reanalyses using contemporary satellite data, *J. Geophys. Res.-Atmos.*, 117, D16105, <https://doi.org/10.1029/2012jd017640>, 2012.
- Liu, X. and Penner, J. E.: Ice nucleation parameterization for global models, *Meteorol. Z.*, 14, 499–514, 2005.
- Liu, X. and Shi, X.: Sensitivity of homogeneous ice nucleation to aerosol perturbations and its implications for aerosol indirect effects through cirrus clouds, *Geophys. Res. Lett.*, 45, 1684–1691, 2018.
- Liu, X., Penner, J. E., and Herzog, M.: Global modeling of aerosol dynamics: Model description, evaluation, and interactions between sulfate and nonsulfate aerosols, *J. Geophys. Res.-Atmos.*, 110, D18206, <https://doi.org/10.1029/2004JD005674>, 2005.
- Liu, X., Easter, R. C., Ghan, S. J., Zaveri, R., Rasch, P., Shi, X., Lamarque, J.-F., Gettelman, A., Morrison, H., Vitt, F., Conley, A., Park, S., Neale, R., Hannay, C., Ekman, A. M. L., Hess, P., Mahowald, N., Collins, W., Iacono, M. J., Bretherton, C. S., Flanner, M. G., and Mitchell, D.: Toward a minimal representation of aerosols in climate models: description and evaluation in the Community Atmosphere Model CAM5, *Geosci. Model Dev.*, 5, 709–739, <https://doi.org/10.5194/gmd-5-709-2012>, 2012.
- Lohmann, U.: Possible aerosol effects on ice clouds via contact nucleation, *J. Atmos. Sci.*, 59, 647–656, 2002.
- Lohmann, U., von Salzen, K., McFarlane, N., Leighton, H. G., and Feichter, J.: Tropospheric sulfur cycle in the Canadian general circulation model, *J. Geophys. Res.-Atmos.*, 104, 26833–26858, 1999.
- Mahrt, F., Kilchhofer, K., Marcolli, C., Grönquist, P., David, R. O., Rösch, M., Lohmann, U., and Kanji, Z. A.: The Impact of Cloud Processing on the Ice Nucleation Abilities of Soot Particles at Cirrus Temperatures, *J. Geophys. Res.-Atmos.*, 125, e2019JD030922, <https://doi.org/10.1029/2019JD030922>, 2019.
- Matus, A. V. and L'Ecuyer, T. S.: The role of cloud phase in Earth's radiation budget, *J. Geophys. Res.-Atmos.*, 122, 2559–2578, 2017.



- Pajunoja, A., Malila, J., Hao, L. Q., Joutsensaari, J., Lehtinen, K. E. J., and Virtanen, A.: Estimating the Viscosity Range of SOA Particles Based on Their Coalescence Time, *Aerosol Sci. Technol.*, 48, I–IV, <https://doi.org/10.1080/02786826.2013.870325>, 2014.
- Penner, J. E., Chen, Y., Wang, M., and Liu, X.: Possible influence of anthropogenic aerosols on cirrus clouds and anthropogenic forcing, *Atmos. Chem. Phys.*, 9, 879–896, <https://doi.org/10.5194/acp-9-879-2009>, 2009.
- Penner, J. E., Zhou, C., Garnier, A., and Mitchell, D. L.: Anthropogenic Aerosol Indirect Effects in Cirrus Clouds, *J. Geophys. Res.-Atmos.*, 123, 11652–611677, <https://doi.org/10.1029/2018jd029204>, 2018.
- Podglajen, A., Hertzog, A., Plougonven, R., and Legras, B.: Lagrangian temperature and vertical velocity fluctuations due to gravity waves in the lower stratosphere, *Geophys. Res. Lett.*, 43, 3543–3553, 2016.
- Pratt, K. A., Murphy, S. M., Subramanian, R., DeMott, P. J., Kok, G. L., Campos, T., Rogers, D. C., Prenni, A. J., Heymsfield, A. J., Seinfeld, J. H., and Prather, K. A.: Flight-based chemical characterization of biomass burning aerosols within two prescribed burn smoke plumes, *Atmos. Chem. Phys.*, 11, 12549–12565, <https://doi.org/10.5194/acp-11-12549-2011>, 2011.
- Prenni, A. J., DeMott, P. J., Sullivan, A. P., Sullivan, R. C., Kreidenweis, S. M., and Rogers, D. C.: Biomass burning as a potential source for atmospheric ice nuclei: Western wildfires and prescribed burns, *Geophys. Res. Lett.*, 39, L11805, <https://doi.org/10.1029/2012GL051915>, 2012.
- Renbaum-Wolff, L., Grayson, J. W., Bateman, A. P., Kuwata, M., Sellier, M., Murray, B. J., Shilling, J. E., Martin, S. T., and Bertram, A. K.: Viscosity of alpha-pinene secondary organic material and implications for particle growth and reactivity, *P. Natl. Acad. Sci. USA*, 110, 8014–8019, <https://doi.org/10.1073/pnas.1219548110>, 2013.
- Richardson, M. S., DeMott, P. J., Kreidenweis, S. M., Cziczo, D. J., Dunlea, E. J., Jimenez, J. L., Thomson, D. S., Ashbaugh, L. L., Borys, R. D., Westphal, D. L., Casuccio, G. S., and Lersch, T. L.: Measurements of heterogeneous ice nuclei in the western United States in springtime and their relation to aerosol characteristics, *J. Geophys. Res.-Atmos.*, 112, D02209, <https://doi.org/10.1029/2006jd007500>, 2007.
- Saukko, E., Lambe, A. T., Massoli, P., Koop, T., Wright, J. P., Croasdale, D. R., Pedernera, D. A., Onasch, T. B., Laaksonen, A., Davidovits, P., Worsnop, D. R., and Virtanen, A.: Humidity-dependent phase state of SOA particles from biogenic and anthropogenic precursors, *Atmos. Chem. Phys.*, 12, 7517–7529, <https://doi.org/10.5194/acp-12-7517-2012>, 2012.
- Shi, X. and Liu, X.: Sensitivity Study of Anthropogenic Aerosol Indirect Forcing through Cirrus Clouds with CAM5 Using Three Ice Nucleation Parameterizations, *J. Meteorol. Res.*, 32, 693–706, <https://doi.org/10.1007/s13351-018-8011-z>, 2018.
- Shi, X., Liu, X., and Zhang, K.: Effects of pre-existing ice crystals on cirrus clouds and comparison between different ice nucleation parameterizations with the Community Atmosphere Model (CAM5), *Atmos. Chem. Phys.*, 15, 1503–1520, <https://doi.org/10.5194/acp-15-1503-2015>, 2015.
- Shiraiwa, M., Li, Y., Tsimpidi, A. P., Karydis, V. A., Berke-meier, T., Pandis, S. N., Lelieveld, J., Koop, T., and Pöschl, U.: Global distribution of particle phase state in atmospheric secondary organic aerosols, *Nat. Commun.*, 8, 15002, <https://doi.org/10.1038/ncomms15002>, 2017.
- Storelvmo, T.: Aerosol Effects on Climate via Mixed-Phase and Ice Clouds, *Annu. Rev. Earth Planet. Sc.*, 45, 199–222, <https://doi.org/10.1146/annurev-earth-060115-012240>, 2017.
- Tilmes, S., Lamarque, J.-F., Emmons, L. K., Kinnison, D. E., Marsh, D., Garcia, R. R., Smith, A. K., Neely, R. R., Conley, A., Vitt, F., Val Martin, M., Tanimoto, H., Simpson, I., Blake, D. R., and Blake, N.: Representation of the Community Earth System Model (CESM1) CAM4-chem within the Chemistry-Climate Model Initiative (CCMI), *Geosci. Model Dev.*, 9, 1853–1890, <https://doi.org/10.5194/gmd-9-1853-2016>, 2016.
- van Marle, M. J. E., Kloster, S., Magi, B. I., Marlon, J. R., Daniau, A.-L., Field, R. D., Arneeth, A., Forrest, M., Hantson, S., Kehrwald, N. M., Knorr, W., Lasslop, G., Li, F., Mangenon, S., Yue, C., Kaiser, J. W., and van der Werf, G. R.: Historic global biomass burning emissions for CMIP6 (BB4CMIP) based on merging satellite observations with proxies and fire models (1750–2015), *Geosci. Model Dev.*, 10, 3329–3357, <https://doi.org/10.5194/gmd-10-3329-2017>, 2017.
- Wagner, R., Höhler, K., Huang, W., Kiselev, A., Möhler, O., Mohr, C., Pajunoja, A., Saathoff, H., Schiebel, T., Shen, X., and Virtanen, A.: Heterogeneous ice nucleation of  $\alpha$ -pinene SOA particles before and after ice cloud processing, *J. Geophys. Res.-Atmos.*, 122, 4924–4943, <https://doi.org/10.1002/2016jd026401>, 2017.
- Waliser, D. E., Li, J. L. F., Woods, C. P., Austin, R. T., Bacmeister, J., Chern, J., Del Genio, A., Jiang, J. H., Kuang, Z., and Meng, H.: Cloud ice: A climate model challenge with signs and expectations of progress, *J. Geophys. Res.-Atmos.*, 114, D00A21, <https://doi.org/10.1029/2008JD010015>, 2009.
- Wang, B., Lambe, A. T., Massoli, P., Onasch, T. B., Davidovits, P., Worsnop, D. R., and Knopf, D. A.: The deposition ice nucleation and immersion freezing potential of amorphous secondary organic aerosol: Pathways for ice and mixed-phase cloud formation, *J. Geophys. Res.-Atmos.*, 117, D16209, <https://doi.org/10.1029/2012JD018063>, 2012.
- Wang, M. and Penner, J. E.: Aerosol indirect forcing in a global model with particle nucleation, *Atmos. Chem. Phys.*, 9, 239–260, <https://doi.org/10.5194/acp-9-239-2009>, 2009.
- Wang, M. and Penner, J. E.: Cirrus clouds in a global climate model with a statistical cirrus cloud scheme, *Atmos. Chem. Phys.*, 10, 5449–5474, <https://doi.org/10.5194/acp-10-5449-2010>, 2010.
- Wang, M., Liu, X., Zhang, K., and Comstock, J. M.: Aerosol effects on cirrus through ice nucleation in the Community Atmosphere Model CAM5 with a statistical cirrus scheme, *J. Adv. Model. Earth Sy.*, 6, 756–776, <https://doi.org/10.1002/2014ms000339>, 2014.
- Wang, P. H., Minnis, P., McCormick, M. P., Kent, G. S., and Skeens, K. M.: A 6-year climatology of cloud occurrence frequency from Stratospheric Aerosol and Gas Experiment II observations (1985–1990), *J. Geophys. Res.-Atmos.*, 101, 29407–29429, 1996.
- Wilkerson, J. T., Jacobson, M. Z., Malwitz, A., Balasubramanian, S., Wayson, R., Fleming, G., Naiman, A. D., and Lele, S. K.: Analysis of emission data from global commercial aviation: 2004 and 2006, *Atmos. Chem. Phys.*, 10, 6391–6408, <https://doi.org/10.5194/acp-10-6391-2010>, 2010.
- Wilson, T. W., Murray, B. J., Wagner, R., Möhler, O., Saathoff, H., Schnaiter, M., Skrotzki, J., Price, H. C., Malkin, T. L., Dobbie, S.,

- and Al-Jumur, S. M. R. K.: Glassy aerosols with a range of compositions nucleate ice heterogeneously at cirrus temperatures, *Atmos. Chem. Phys.*, 12, 8611–8632, <https://doi.org/10.5194/acp-12-8611-2012>, 2012.
- Yun, Y., Penner, J. E., and Popovicheva, O.: The effects of hygroscopicity on ice nucleation of fossil fuel combustion aerosols in mixed-phase clouds, *Atmos. Chem. Phys.*, 13, 4339–4348, <https://doi.org/10.5194/acp-13-4339-2013>, 2013.
- Zender, C. S., Bian, H., and Newman, D.: Mineral Dust Entrainment and Deposition (DEAD) model: Description and 1990s dust climatology, *J. Geophys. Res.*, 108, 4416, <https://doi.org/10.1029/2002JD002775>, 2003.
- Zhang, K., Wan, H., Liu, X., Ghan, S. J., Kooperman, G. J., Ma, P.-L., Rasch, P. J., Neubauer, D., and Lohmann, U.: Technical Note: On the use of nudging for aerosol–climate model intercomparison studies, *Atmos. Chem. Phys.*, 14, 8631–8645, <https://doi.org/10.5194/acp-14-8631-2014>, 2014.
- Zhou, C. and Penner, J. E.: Aircraft soot indirect effect on large-scale cirrus clouds: Is the indirect forcing by aircraft soot positive or negative?, *J. Geophys. Res.-Atmos.*, 119, 11303–11320, <https://doi.org/10.1002/2014jd021914>, 2014.
- Zhou, C., Penner, J. E., Lin, G., Liu, X., and Wang, M.: What controls the low ice number concentration in the upper troposphere?, *Atmos. Chem. Phys.*, 16, 12411–12424, <https://doi.org/10.5194/acp-16-12411-2016>, 2016.
- Zhu, J. and Penner, J. E.: Global Modeling of Secondary Organic Aerosol With Organic Nucleation, *J. Geophys. Res.-Atmos.*, 124, 8260–8286, 2019.
- Zhu, J. and Penner, J. E.: Indirect effects of secondary organic aerosol on cirrus clouds, *J. Geophys. Res.-Atmos.*, 125, e2019JD032233, <https://doi.org/10.1029/2019JD032233>, 2020.
- Zhu, J., Penner, J. E., Lin, G., Zhou, C., Xu, L., and Zhuang, B.: Mechanism of SOA formation determines magnitude of radiative effects, *P. Natl. Acad. Sci. USA*, 114, 12685–12690, <https://doi.org/10.1073/pnas.1712273114>, 2017.
- Zhu, J., Penner, J. E., Yu, F., Sillman, S., Andreae, M. O., and Coe, H.: Decrease in radiative forcing by organic aerosol nucleation, climate, and land use change, *Nat. Commun.*, 10, 423, <https://doi.org/10.1038/s41467-019-08407-7>, 2019.